






Article

Effect of Wear-Corrosion of Reduced Graphene Oxide Functionalized with Hyaluronic Acid on Inflammatory and Proteomic Response of J774A.1 Macrophages

Luna Sánchez-López ^{1,2,3} , Noelia Ropero de Torres ¹, Belén Chico ² , Natalia Soledad Fagali ⁴ , Vivian de los Ríos ¹ , María Lorenza Escudero ², María Cristina García-Alonso ^{2,*}  and Rosa María Lozano ^{1,*} 

¹ Centro de Investigaciones Biológicas-Margarita Salas (CIB Margarita Salas), Consejo Superior de Investigaciones Científicas (CSIC), 28040 Madrid, Spain; luna.sanchez@cenim.csic.es (L.S.-L.); noelia.sbe@gmail.com (N.R.d.T.); vrios@cib.csic.es (V.d.l.R.)

² Centro Nacional de Investigaciones Metalúrgicas (CENIM), Consejo Superior de Investigaciones Científicas (CSIC), 28040 Madrid, Spain; bchico@cenim.csic.es (B.C.); escudero@cenim.csic.es (M.L.E.)

³ PhD Program in Advanced Materials and Nanotechnology, Doctoral School, Universidad Autónoma de Madrid, Ciudad Universitaria de Cantoblanco, 28049 Madrid, Spain

⁴ Instituto de Investigaciones Fisicoquímicas Teóricas y Aplicadas (INIFTA), Universidad Nacional de La Plata (UNLP), Consejo Nacional de Investigaciones Científicas y Técnicas (CONICET), La Plata 1900, Argentina; nfagali@inifta.unlp.edu.ar

* Correspondence: crisga@cenim.csic.es (M.C.G.-A.); rlozano@cib.csic.es (R.M.L.)

Abstract: The presence of a worn surface in the implanted material, as in the case of a replacement of a damaged osteoarticular joint, is the normal condition after implantation. This manuscript focuses precisely on the comparative study of the cellular behavior on worn CoCr surfaces, analyzing the effect of different surface modifications on macrophages' responses. CoCr surfaces were modified by the deposition of electrochemically reduced graphene oxide (CoCrErGO), followed by additional surface functionalization with hyaluronic acid (CoCrErGOHA). After the wear corrosion processes, the macrophage response was studied. In addition, macrophage supernatants exposed to the surfaces, before and after wear, were also evaluated for osteoblast response through the analysis of the metabolic activity, plasma membrane damage, and phosphatase alkaline activity (ALP). The proteomic analysis and the quantitative TNF- α /IL-10 ratios of the J774A.1 macrophages exposed to the surfaces under study showed a polarization shift from M0 (basal state) to M1, associated with the pro-inflammatory response of all surfaces. A lower M1 polarization was observed upon exposure to the surface modification with ErGO, whereas posterior HA functionalization attenuated, even more, the M1 polarization. The wear corrosion process contributed to inflammation and exacerbated the M1 polarization response on macrophages to CoCr, which was diminished for the ErGO and attenuated the most for the ErGOHA surfaces. Comparative proteomics showed that the pathways related to M1 polarization were downregulated on the surfaces of CoCrErGOHA, which suggests mechanisms for the observed attenuation of M1 polarization. The suitable immuno-modulatory potential induced by the ErGOHA surface, with and without wear, together with the stimulation of ALP activity in osteoblasts induced by macrophage supernatants, promotes the mineralization processes necessary for bone repair. This makes it feasible to consider the adsorption of ErGOHA on CoCr as a recommended surface treatment for the use of biomaterials in osseous joint applications.

Keywords: CoCr; proteomic analysis; inflammatory response; wear; graphene; hyaluronic acid



Citation: Sánchez-López, L.; Ropero de Torres, N.; Chico, B.; Soledad Fagali, N.; de los Ríos, V.; Escudero, M.L.; García-Alonso, M.C.; Lozano, R.M. Effect of Wear-Corrosion of Reduced Graphene Oxide Functionalized with Hyaluronic Acid on Inflammatory and Proteomic Response of J774A.1 Macrophages. *Metals* **2023**, *13*, 598. <https://doi.org/10.3390/met13030598>

Academic Editor: David M. Bastidas

Received: 30 January 2023

Revised: 3 March 2023

Accepted: 9 March 2023

Published: 15 March 2023



Copyright: © 2023 by the authors. Licensee MDPI, Basel, Switzerland. This article is an open access article distributed under the terms and conditions of the Creative Commons Attribution (CC BY) license (<https://creativecommons.org/licenses/by/4.0/>).

1. Introduction

The implantation of biomaterials within the body initiates a series of immune reactions, collectively called the biomaterial-based foreign body response (B-FBR), which promotes the isolation of the implanted foreign material from the host immune system. This response limits the longevity and functionality of many biomedical implants. In the case of CoCr

joint replacements, if the chronic inflammation is not resolved after the implantation, bone resorption occurs, leading to implant loosening and eventually the failure of the prosthesis.

Upon implantation of any biomaterial, the adsorption of serum proteins occurs on the material surface in the first place. This is similar to the formation of the protein corona on the surface of particles produced in the wear corrosion processes. The nature of the adsorbed proteins on the biomaterial surface, in turn, determines the following events, i.e., activation of the coagulation and complement cascades, and the recruitment of immune cells [1]. Neutrophils are the first innate immune cells recruited for infiltration, followed by macrophages, which will try to engulf and degrade the foreign material. If the elimination of the foreign biomaterial is not possible and frustrated phagocytosis occurs, macrophages will fuse to form foreign body giant cells (FBGCs), which will try to degrade the material by secreting reactive oxygen species (ROS) and degradative enzymes [2]. Hence, macrophages are considered key regulators of the FBR in biomaterials.

It is reported that wear debris stimulates chronic inflammation and bone destruction that may ultimately result in implant loosening. Macrophages, as sentinel cells of the innate immunity system, are central to the initiation of this inflammatory cascade via the release of pro-inflammatory and pro-osteoclastic factors. Like the response to pathogens, wear particles elicit a macrophage response based on the unique properties of the cells belonging to this lineage, including sensing, chemotaxis, phagocytosis, and adaptive stimulation.

Macrophages consist of a heterogeneous population of cells, which might be activated through polarization towards the classically activated M1 phenotype or the alternative M2 phenotype. The M1 phenotype is associated with the pro-inflammatory response against pathogens, while the M2 phenotype is associated with immunoregulation and tissue regeneration responses [3]. However, the reality is that macrophage polarization is far more complex, and macrophages exist in a continuum of activation states between the M1/M2 polarization spectrum, meaning that M1 and M2 phenotypes are the most polarized phenotypes at the opposite extremes of the spectrum. Some M2 sub-phenotypes have been further characterized (M2 a–d), as well as other disease-related M2 phenotypes (M2_{eff}, M4, or MHem) [4]. In addition to macrophage phenotypic heterogeneity, the macrophage's plasticity ability allows them to switch among phenotypes depending on the current signaling signals presented in their microenvironment, therefore varying their M1/M2 profile ratios [5]. In fact, the macrophage polarization stage plays a determinant role in the outcome of an implant.

Biomaterials that trigger an M1 response have been associated with chronic biomaterial-based FBR, chronic inflammation, and chronic fibrosis leading to fibrotic encapsulation of the implant. On the other hand, the M2 phenotype has been associated with supporting vascularization and organized tissue remodeling, favoring the integration of the biomaterial [6]. Therefore, the type of interaction of macrophages with the biomaterial surface strongly determines the success and functional durability of the implant. For that reason, the manufacture of immunomodulatory biomaterials that modulate macrophage polarization towards the M2 phenotype is essential for the long-term survival and function of the implanted biomedical devices [2]. One strategy to reach this objective is the modification of the biomaterial surface chemistry to encourage a favorable interaction at the macrophage/material interface. In fact, the application of surface coatings on the surface of biomaterials has reduced the amount of M1 activation while increasing the M2 to M1 ratio and has also reduced FBGC formation [7]. Further modification of the surface chemistry of biomaterials through biomolecular strategies might also be applied. The incorporation of biomolecules may modulate the immune response via the specific biomaterial's interaction with cell receptors.

According to this, the macrophages responding to tissue injury are activated by the inflammatory signals in their microenvironment and developed into classically activated M1 macrophages, which release mediators that are important in host defense, such as TNF- α , or, alternatively, activated M2 macrophages, which generate products that downregulate the inflammatory response, such as IL-10. The induction of M1/M2 polarization by bioma-

materials remains controversial, which might be due to the basic characterization techniques used. Two hypotheses have been proposed for these phenomena. Some researchers claim that these FBR-associated macrophages may have a hybrid phenotype, co-expressing M1 and M2 markers, which may indicate a transitional state between M1 and M2 phenotypes. On the other hand, other authors argue that both M1 and M2 macrophages are present in the implant surroundings at various ratios that change over time in a spatiotemporal-dependent manner [2,7]. Both hypotheses are difficult to demonstrate with conventionally applied technologies, where comprehensive phenotyping characterization is not possible due to technological limitations, since a limited number of concurrent markers can be analyzed at once by flow cytometry techniques, and a limited number of antibodies can also be applied in histology studies [2]. Advances in new omics technologies that allow massive expression analysis, such as transcriptomics or proteomics, may provide a more comprehensive perspective regarding the whole macrophage polarization spectrum and the intermediate stages repertoire; in fact, more exhaustive polarization knowledge is also required to design improved, next-generation immunomodulatory materials.

Although the scientific literature has numerous articles concerning the effect of wear debris of CoCr on cells [8,9], there are no studies so far that deal with the cellular response to the worn surface itself. The presence of worn zones on the surfaces of the joint replacement is the habitual condition after implantation. This manuscript focuses precisely on the study of the cellular response to worn CoCr surfaces, analyzing the effect of different surface modifications. Since the interactions between cells and biomaterials occur primarily at the cell-biomaterial interface, modification of physicochemical properties at the biomaterial surface allows the modulation of the cellular response while preserving the required mechanical bulk properties of metal prostheses. ErGO and ErGOHA functionalization were previously performed in our group to increase lubrication in joint prostheses due to the lubricant characteristics of graphene and HA. In their publication, the authors show that the chemical modification of the CoCr surface with ErGO revealed increased macrophage biocompatibility when compared to the bare CoCr surface [10]. Additional functionalization of the surface with HA increased the macrophage biocompatibility even more compared to CoCrErGO. A beneficial change in the inflammatory macrophage response was observed with increased production of the anti-inflammatory cytokine IL-10 [11]. In addition, functionalization with HA may provide further cytoprotective effects upon the wear corrosion phenomena of a CoCr surface, since HA has been shown to decrease the cytotoxicity of CoCr wear particles [9].

In this work, a high-throughput proteomic approach was carried out to analyze the effect of surface modification and worn surfaces on the macrophage cellular response, in the same way as the degradation process occurs in implanted joint prostheses, to identify patterns of protein expression that could serve as biomarkers to select the most tolerable material. The proteomic results were correlated with the inflammatory response induced by the effect of wear on CoCr and their surface modifications by ErGO and ErGOHA, measuring the levels of TNF- α and IL-10 in macrophages and using the TNF- α /IL-10 ratio for each material as a measurement of the macrophage inflammatory balance between phenotype M1 and M2. Additionally, macrophage supernatants exposed to CoCr with surface modifications, before and after the wear corrosion test, were also analyzed here on the response of MC3T3-E1 pre-osteoblast cultures in order to analyze the consequences of the cytokines released by macrophages in bone repair.

2. Materials and Methods

2.1. Materials

Biomedical grade CoCr alloy for this study was provided by International Edge with the following chemical composition (wt.%): 27.25% Cr, 5.36% Mo, 0.69% Mn, 0.68% Si, 0.044% C, 0.02% W, 0.15% N, 0.002% Al, 0.001% S, 0.002% P, 0.002% B, 0.001% Ti, balance Co.

CoCr disks of 38 mm diameter and 3 mm thickness were polished on successive abrasive papers in silicon carbide grade from 600 to 2000, finally polished with 3 μm and 1 μm diamond paste, and subsequently washed with distilled water.

2.2. Electrochemically Reduced Graphene Oxide and Functionalization with Hyaluronic Acid on CoCr Surfaces

2.2.1. Electrochemical Reduction of Graphene Oxide on CoCr Disks (CoCrErGO)

CoCr surfaces were immersed in an aqueous solution of GO (4 g/L) immediately after polishing, and direct electrochemical reduction of the graphene oxide (GO) on the CoCr surfaces was performed. CoCr disks were used as working electrodes, a graphite bar was used as the auxiliary electrode, and an Ag/AgCl (3M KCl) electrode was used as a reference. An Autolab32 potentiostat/galvanostat was used for the electrochemical experiments. The electrochemical method used to synthesize the reduced GO films on CoCr surfaces was cyclic voltammetry (CV). The potential applied to CoCr disks to deposit the reduced graphene oxide varied from $-2.1 \text{ V}_{\text{vs. Ag/AgCl}}$ to $-0.5 \text{ V}_{\text{vs. Ag/AgCl}}$ at a scanning rate of 10 mV/s for 5 consecutive cycles [12]. The potential window assures the electrochemical reduction of graphene oxide on CoCr surfaces. The obtained modified surfaces were hereafter denominated CoCrErGO.

2.2.2. Functionalization of ErGO with HA (CoCrErGOHA)

The CoCrErGO surfaces were washed with distilled water and further functionalized with HA (hyaluronic acid, 53747, Sigma-Aldrich Chemie GmbH, Schnellendorf, Germany), which will be called CoCrErGOHA from now on. Functionalization was carried out by soaking CoCrErGO samples for 24 h in a phosphate buffer saline (PBS) solution of the following chemical composition: 0.2 g/L KCl, 0.2 g/L KH_2PO_4 , 8 g/L NaCl, and 1.150 g/L Na_2HPO_4 anhydrous, and containing 3 g/L of HA, the concentration equivalent of that found in the synovial fluid [13].

2.3. Wear Corrosion Tests

Wear corrosion tests were performed using a pin-on-disk tribometer. Disks of 38 mm diameter of CoCr, CoCrErGO, and CoCrErGOHA were tested in contact with a CoCr cylinder of 7 mm diameter as their counterpart (pin). A normal load of 5 N at a rotation rate of 120 rpm for 30,000 m was applied. Wear corrosion tests were performed in simulated synovial fluid composed of a PBS solution containing 3 g/L HA that was recirculating during the test. Wear corrosion tests were performed in a recirculating phosphate buffer saline (PBS) solution containing 3 g/L HA. Wear corrosion tests for each surface were done in triplicate. A characterization by optical microscopy (OM) and scanning electron microscopy (SEM/EDX) was carried out after the wear corrosion tests.

2.4. Macrophage Assays

2.4.1. Macrophage Cell Cultures

The mouse macrophage J774A.1 cell line was provided by the DSMZ Human and Animal Cell Bank (DSMZ, Braunschweig, Germany). Cells were cultured in cell culture medium (Dulbecco's Modified Eagle Medium, DMEM 41966; Gibco ThermoFisher Scientific, Waltham, MA, USA) supplemented with 10% heat-inactivated fetal bovine serum (FBS; Gibco ThermoFisher Scientific, Waltham, MA, USA) and with a mixture of antibiotics (penicillin at 100 units/mL and streptomycin at 100 $\mu\text{g}/\text{mL}$, Gibco, BRL), hereafter referred to as "complete cell culture medium".

Prior to the cell culture assays, both sides of the metallic disks were sterilized for 5 min under UV in an active vertical flux cabin. After sterilization, disks were introduced in a sterile tissue culture dish with the following dimensions: 60 \times 15 mm (BD, 1 Becton Drive, NJ, USA), where macrophage culture was seeded. In the case of disks that undergo wear corrosion tests, the worn surface was facing up in the dish. In each assay, three culture dishes were used: one as a control (with no material, group named "Control"), another with

one disk of CoCr, CoCrErGO, and CoCrErGOHA surfaces without wear (group named “no wear”) that had been previously incubated for four days in the PBS-HA solution as used in tribocorrosion tests, and the last one with one disk of CoCr, CoCrErGO, or CoCrErGOHA after tribocorrosion tests (group named “with wear”). Macrophage cultures were seeded at a cell density of 12,500 cells/cm² for 72 h and 10,000 cells/cm² for 96 h cell cultures in a culture dish that had a culture area of 19.5 cm², in 7 mL of complete cell culture medium, and incubated in a cell culture chamber at 37 °C and 5% CO₂.

2.4.2. Inflammatory Response of J774A.1 Macrophages

After culture, cell medium (here named “supernatant”) was collected, centrifuged for 5 min at 1024× *g*, and maintained as aliquots at −20 °C. Quantitative determination of murine tumor necrosis factor- α (TNF- α) and interleukin-10 (IL-10) was measured with commercial kits specifically for their detection: the murine TNF- α Elisa Kit (Diacclone, Besançon, France) and Murine IL-10 Elisa Kit (Diacclone, Besançon, France). Protein concentration measured in cell extracts (described below) was used for the normalization of cytokine concentrations between samples studied.

2.4.3. Macrophages Culture Extracts for Proteomic Analysis

After incubation assays, cells were then washed with 10 mL of ice-cold PBS and aspirated to remove the excess PBS. Plates were kept on ice during all steps. Cells grown on every disk surface and every culture dish were lysed in a 5 mL RIPA lysis buffer kit (Santa Cruz Biotechnology, Santa Cruz, CA, USA) that contained the following protease inhibitors: 2 mM of phenylmethylsulfonyl fluoride (PMSF), 1 mM sodium orthovanadate, and a dilution of 1:100 protease inhibitor cocktail are provided in the kit. Protease inhibitors protect proteins from proteolytic degradation through the inhibition of the serine-proteases, cysteine-proteases, aspartic acid-proteases, and aminopeptidases that are typically present in cellular lysate samples. Cells were scraped (Sarstedt, NC, USA) and transferred to a 15 mL conical tube, and the lysates were incubated with RIPA lysis buffer on ice for 15 min. Then, cellular lysates were sonicated (Branson 1510, set at 50% amplitude) three times for two seconds each, with at least one-minute of rest on ice between each two-second pulse. Then, lysates were incubated on ice for an additional 15 min to increase protein extraction yield and centrifuged at 12,100× *g* for 5 min at 4 °C, collecting the supernatants into Eppendorf microtubes and stored in aliquots at −20 °C avoiding multiple freeze/thaw cycles. The protein concentration of each supernatant from each lysed cell was evaluated (Thermo Scientific™ Pierce™ 660 nm protein assay, Pierce Biotechnology, Rockford, IL, USA) by a colorimetric method for total protein quantification.

2.5. Proteomic Analysis

2.5.1. Sample Preparation for Proteomic Analysis

60 μ g of total protein from each cell extract was precipitated with cold acetone (−20 °C) (CHROMASOL V[®]Plus, for HPLC, \geq 99.9%; Sigma-Aldrich, Burlington, MA, USA). The precipitated protein was resuspended in 20 μ L of loading buffer and loaded into a 10% acrylamide/bisacrilamide SDS/PAGE gel. Gels were run until the whole proteome had penetrated the resolving gel (about 1 cm of total migration). Gels were stained with the Colloidal Blue Staining Kit (Invitrogen, Thermo Fisher Scientific, Waltham, MA, USA). Each proteome was excised and cut into small pieces before manual in-gel digestion with trypsin. Excised bands were separately destained with 50 mM ammonium bicarbonate (ABC; Sigma-Aldrich, Burlington, MA, USA) and 50% acetonitrile (ACN; Fisher Chemical, Waltham, MA, USA). Samples were then reduced with 10 mM dithiothreitol (BIO-RAD, Hercules, CA, USA) in 50 mM ABC and alkylated with 55 mM iodoacetamide (GE Healthcare Life Sciences, Marlborough, MA, USA) in 50 mM ABC. Then, gel pieces were digested with porcine trypsin (Pierce, Thermo Fisher Scientific, Waltham, MA, USA), at a final concentration of 12.5 ng/ μ L in 50 mM ABC, overnight at 37 °C. Peptides were extracted using 100% ACN and 0.5% trifluoroacetic acid (Sigma-Aldrich, Burlington, MA, USA),

purified using a Zip Tip (Millipore, Sigma-Aldrich, Burlington, MA, USA), and dried [14]. Finally, samples were reconstituted in 12 μ L of 0.1% formic acid (Fisher Chemical, Waltham, MA, USA), and the peptide quantification was performed using the Qubit[®] Protein Assay Kit and the Qubit[®] 4.0 fluorometer.

2.5.2. LC-MS Analysis

All peptide separations were carried out on an Easy-nLC 1000 nanosystem (Thermo Scientific, Waltham, MA, USA). For each analysis, the trypsin-digested peptides were loaded into a precolumn Acclaim PepMap 100 (Thermo Scientific, Waltham, MA, USA) and eluted in a RSLC PepMap C18, 15 cm long, 50 μ m inner diameter, and 2 μ m particle size (Thermo Scientific, Waltham, MA, USA). The mobile phase flow rate was 300 nL/min using 0.1% formic acid in water (solvent A) and 0.1% formic acid and 99.9% acetonitrile (solvent B). The gradient profile was set as follows: 5–35% solvent B for 100 min, 35–45% solvent B for 20 min, 45–100% solvent B for 5 min, and 100% solvent B for 15 min. Four microliters (1 μ g) of each sample were injected.

MS analysis was performed using a Q Exactive mass spectrometer (Thermo Scientific, USA). For ionization, 1900 V of liquid junction voltage and 270 °C capillary temperature were used. The full scan method employed a m/z 300–1800 mass selection, an Orbitrap resolution of 70,000 (at m/z 200), a target automatic gain control (AGC) value of 3×10^6 , and maximum injection times of 100 ms. After the survey scan, the fifteen most intense precursor ions were selected for MS/MS fragmentation. Fragmentation was performed with a normalized collision energy of 27 eV, and MS/MS scans were acquired with a starting mass of m/z 200, an AGC target of 2×10^5 , a resolution of 17,500 (at m/z 200), an intensity threshold of 8×10^4 , an isolation window of 2 m/z units, and a maximum IT of 100 ms. Charge state screening was enabled to reject unassigned, singly charged, and equal to or more than seven protonated ions. A dynamic exclusion time of 30 s was used to discriminate against previously selected ions.

2.5.3. MS Data Analysis

MS data were analyzed with Proteome Discoverer (version 1.4.1.14, Thermo Fisher Scientific, USA) using standardized workflows. Mass spectra *.raw files were searched against the SwissProt_2020_5.fasta, *Mus musculus* (house mouse) database (17053 protein sequence entries) using the Mascot search engine (version 2.6, Matrix Science). Precursor and fragment mass tolerance were set to 10 ppm and 0.02 Da, respectively, allowing for two missed cleavages, carbamidomethylation of cysteines as a fixed modification, methionine oxidation, phosphorylation, and acetylation N-terminal as a variable modification. Identified peptides were filtered using the Percolator algorithm [14] with a q -value threshold of 0.01.

2.5.4. Bioinformatic Analysis of Proteomic Data

After annotation of raw MS data files, annotated MS files were filtered by massive screening using the programming software MATLAB 2020b, which was used for the identification of annotated ID proteins whose pattern of expression was shared between groups at both exposure times, 72 h and 96 h. Venn diagrams were plotted [15] to visualize shared and exclusive protein expressions between groups. Filtered MS files were generated and further used for identifying differentially expressed proteins (DEPs). Log₂ data transformation was performed, followed by computing the norm. The average of the norm values was obtained and used for calculating the correlation slope. Normalization by correlation slope was then performed to normalize protein abundance, followed by the imputation of missing values. Fold change was computed as the average value of two biological replicates. Mean pairwise comparisons were computed with a Student's t -test, following the data flow from [16]. Differentially expressed proteins (DEPs) were considered significant if the p -value was lower than 0.05 and the fold change was larger than 2 (for upregulated DEPs)

or lower than 2 (for downregulated DEPs). Volcano plots represented the \log_2 (fold change) on the x-axis and the \log_{10} (*p*-value) on the y-axis.

Significant upregulated and downregulated DEPs were then assessed by gene ontology enrichment analyses with software ShinyGO 0.76 [17], where the available databases: Biological Process (BP), Molecular Function (MF), Cellular Component (CC), Kyoto Encyclopedia of Genes and Genomes (KEGG), and Curated Reactome, Panther, and Wikipathways, among other mouse datasets, were applied to assess possible enriched standardized gene ontology terms. The FDR cutoff was set to 0.05, and the quantification of enriched terms was based on the enrichment score. The minimum pathway size for a significant enrichment was set to 2 ID proteins. Only statistically significant enrichments of standardized gene ontology terms were considered for up- and downregulations.

2.6. Effect of Macrophages Supernatants on Pre-Osteoblast Cell Response: WST-1, LDH, and Phosphatase Alkaline Assays

Macrophage supernatants were collected under sterile conditions after 72 and 96 h of incubation with the materials in the study: CoCr, CoCrErGO, and CoCrErGOHA, before and after tribocorrosion, and always using as control assay supernatants from cell cultures without any material. Samples were kept frozen at $-20\text{ }^{\circ}\text{C}$ until assays were performed.

The effect of macrophage supernatants was evaluated in mouse pre-osteoblast MC3T3-E1 cell cultures provided by the DSMZ Human and Animal Cell Bank (DSMZ, Braunschweig, Germany). To test the effect of supernatants on the osteoblast cell response, the metabolic activity (Cell Proliferation Reagent WST-1 Assay, Roche, Basel, Switzerland) and plasma membrane damage (Cytotoxicity Detection Kit plus [LDH], Roche, Basel, Switzerland) of osteoblast cultures were evaluated [18].

The effect of macrophage supernatants on pre-osteoblast differentiation, induced by ascorbic acid, dexamethasone, and β -glycerol phosphate, was assessed by the alkaline phosphatase (ALP) activity kit (Alkaline Phosphatase Assay Kit ab83369, Abcam, Waltham, MA, USA).

For WST-1 and LDH assays, pre-osteoblast cells were seeded at a cell density of 200,000 cells/mL on 96-well culture plates in a volume of 100 μL of complete cell culture medium. Cell cultures were maintained for 48 h in a cell culture chamber at $37\text{ }^{\circ}\text{C}$ and 5% CO_2 . Cell culture medium was replaced by 100 μL of macrophage supernatants and incubated for another 24 h. Then, WST-1 and LDH assays were performed as previously described [18]. The percent cytotoxicity was calculated as the LDH assay brochure indicates.

For the ALP assay, pre-osteoblast cells were seeded at a cell density of 60,000 cells/mL on 48-well culture plates in a volume of 0.5 mL of complete cell culture medium. After 48 h of seeding, the complete cell culture medium was removed and replaced by an osteogenic medium to induce cell differentiation that contains 0.1 μM dexamethasone, 0.2 mM ascorbic acid, and 10 mM of β -glycerophosphate in DMEM [19]. The osteogenic medium was replaced by a fresh osteogenic medium every 72 h until reaching 10 days of differentiation. After differentiation time, the cells were incubated with the macrophage supernatants for 24 h. ALP activity was measured with a commercial kit (ab83369, Abcam, Waltham, MA, USA) after washing cells with PBS. All experiments were carried out when cells were between passages five and fifteen. Results were obtained from quadruplicate experiments, and data were expressed as means with standard deviations. Differences between groups were analyzed by one-way analysis of variance (ANOVA), followed by a multiple comparison Bonferroni test. Differences with a *p*-value < 0.01 were considered statistically significant.

3. Results and Discussion

3.1. Tribocorrosion of CoCr, CoCrErGO and CoCrErGOHA

The configuration of the disk/cylinder of metal on the metal used in the tribocorrosion tests was selected to obtain disks with a larger worn area surface than the one obtained when a ball is used as a pin in wear corrosion tests. It is considered essential that the ratio

between wear/intact surface in the disk be as high as possible to evaluate the consequences of wear on inflammatory cell response and cell behavior. Figure 1a–c shows the optical microscopy images of the wear tracks obtained in each material surface after 30,000 m of sliding distance. Using a digital image processing program (Image J), it has been possible to measure the percentage of the worn surface area of each tested surface: (a) CoCr (26%), (b) CoCrErGO (22%), and (c) CoCrErGOHA (17%). The results show an effect of the nature of the metal surface on wear. The lower percentage of the worn surface observed when the metal surface is covered by ErGOHA is due to the lubricant properties of graphene and HA. Figure 1d shows a SEM image of the CoCrErGO surface after the tribocorrosion test. Black carbon-enriched precipitates can be observed accumulating in specific areas of the track.

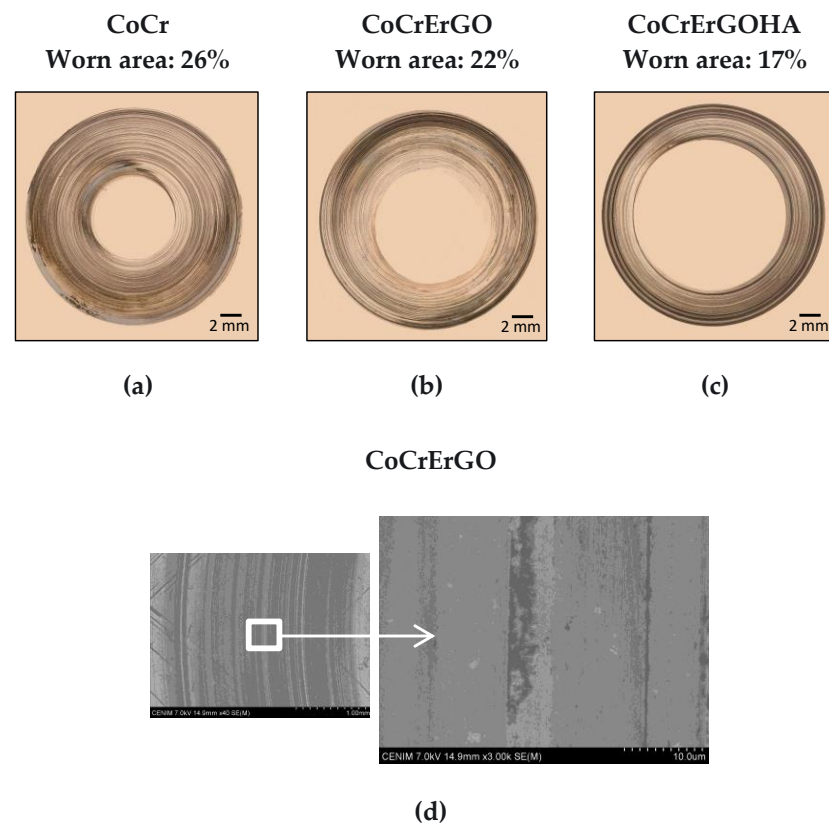


Figure 1. Optical microscopy images of the worn tracks after tribocorrosion tests in CoCr (a), CoCrErGO (b), and CoCrErGOHA (c) after 30,000 m of sliding distance. Scanning electron microscopy image of the worn track after tribocorrosion testing in CoCrErGO (d) after 30,000 m of sliding distance.

3.2. Proteomic Profile of J774A.1 Macrophages in Response to the Modified Surfaces—Effect of Wear

Venn diagrams in Figures 2–4 show the total number of proteins identified in the macrophage proteome that are exclusively expressed in a group or shared between groups after 72 h (a) and 96 h (b) of biomaterial interaction. Panels a and b for each surface show the number of proteins whose expression is shared between the three different groups (control, no wear, and wear as a grey region), the number of proteins that are expressed in two groups (light blue, orange, and pink regions), or the number of proteins that are exclusively expressed in each group (green, red, and dark blue colors) at 72 h (a) or 96 h (b) of exposure to each surface without or with wear. The Venn diagrams at (c) show the intra-group total number of proteins identified in the macrophage proteome in each group, exclusively expressed after 72 h or 96 h, or shared expression at both times of exposure. Volcano plots in panel (d) show the Differentially Expressed Proteins (DEPs) that were upregulated (red) or downregulated (blue) between pairs of groups: no wear vs. control (d1), wear vs. control

(d2), and wear vs. no wear (d3) for each surface. Finally, in Supplementary Figures S1–S3 panel (e), the gene ontology enrichment analysis for no wear (e1), wear vs. control (e2), and wear vs. no wear (e3) is shown for each modified surface.

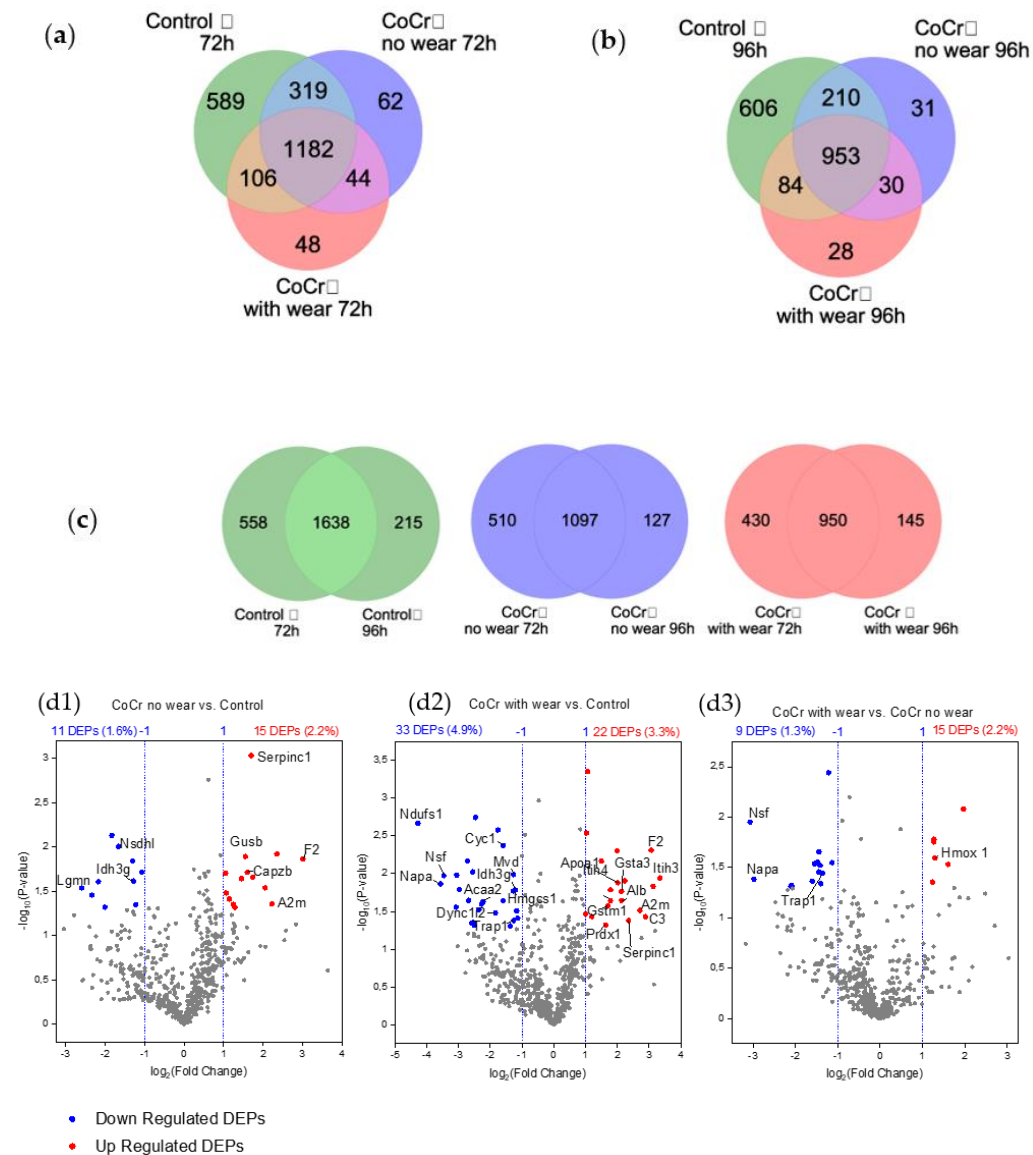


Figure 2. Proteomic profiling of J744A.1 macrophages in response to CoCr-surfaces: (a,b) Inter-group Venn diagrams showing the total number of proteins identified in macrophage proteome exclusively expressed in a group or shared between groups, after 72 h and 96 h of biomaterial interaction; (c) Intra-group Venn diagrams showing the total number of proteins identified in macrophage proteome in each group, exclusively expressed after 72 h or 96 h or shared expression at both times of exposure; (d) Pairwise volcano plots (d1–d3) showing differentially expressed proteins (DEPs) between pairwise group comparisons: CoCr no wear vs. control (d1) CoCr with wear vs. control (d2), CoCr with wear vs. CoCr no wear (d3); Statistically significant DEPs were computed by Student’s t-test pairwise comparisons with a p -value < 0.05.

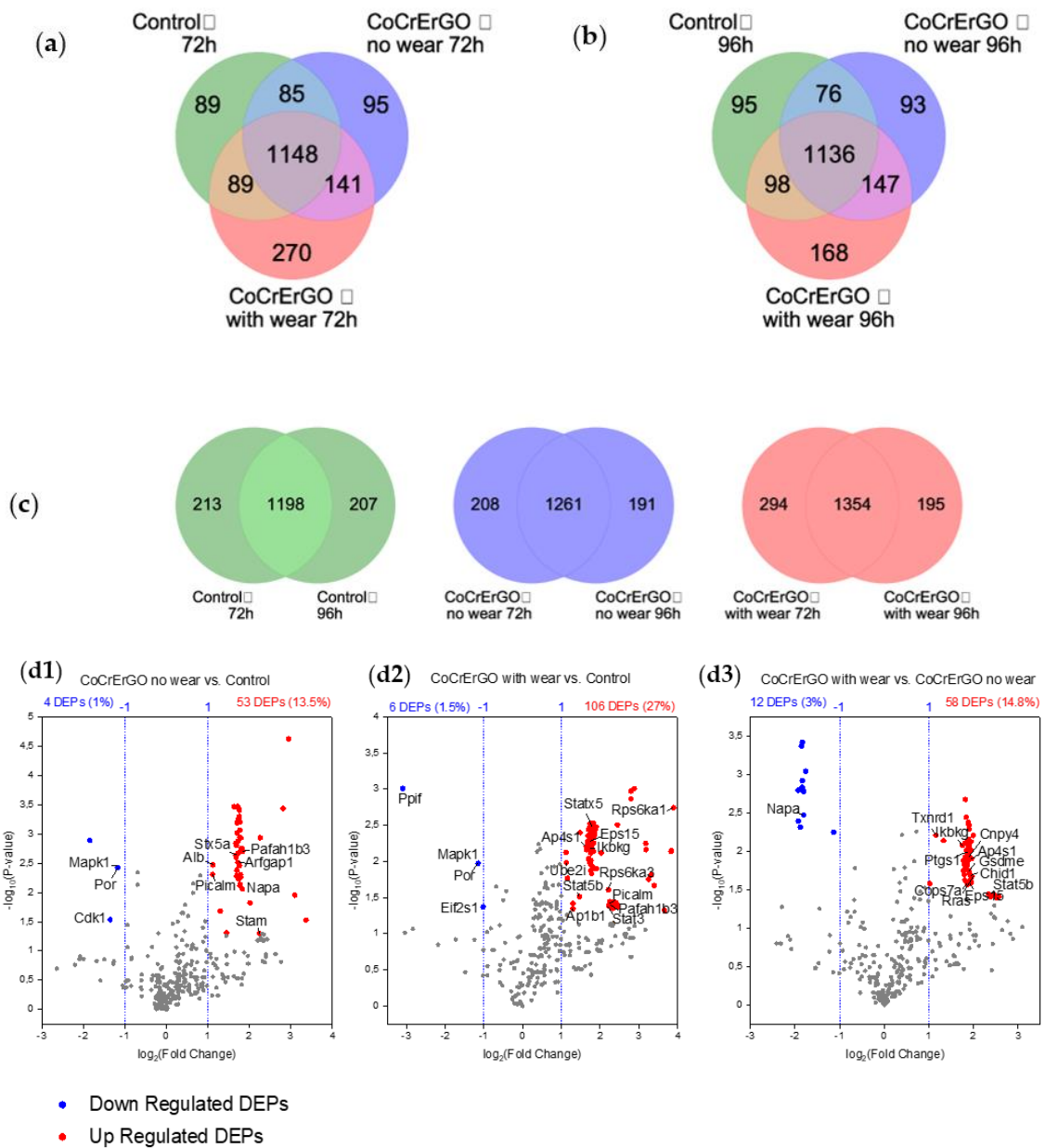


Figure 3. Proteomic profiling of J744A.1 macrophages in response to CoCrErGO surfaces: (a,b) Inter-group Venn diagrams showing the total number of proteins identified in macrophage proteome exclusively expressed in a group or shared between groups, after 72 h and 96 h of biomaterial interaction; (c) Intra-group Venn diagrams showing the total number of proteins identified in macrophage proteome in each group, exclusively expressed after 72 h or 96 h or shared expression at both times of exposure; (d) Pairwise volcano plots (d1–d3) showing differentially expressed proteins (DEPs) between pairwise group comparisons: CoCrErGO no wear vs. control (d1) CoCrErGO with wear vs. control (d2), CoCrErGO with wear vs. CoCrErGO no wear (d3); Statistically significant DEPs were computed by Student’s t-test pairwise comparisons with a *p*-value < 0.05.

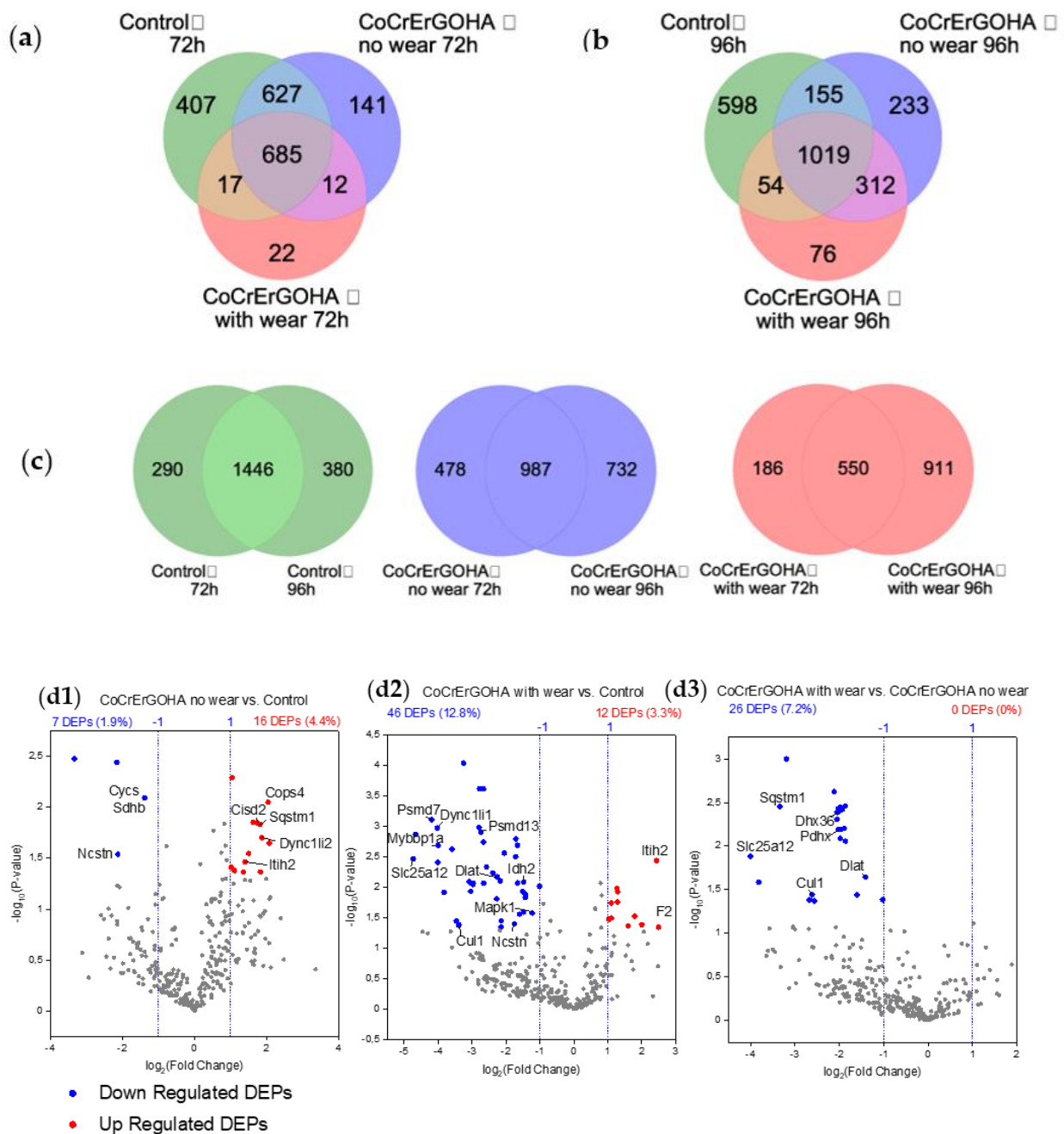


Figure 4. Proteomic profiling of J744A.1 macrophages in response to CoCrErGOHA surfaces: (a,b) Inter-group Venn diagrams showing the total number of proteins identified in macrophage proteome exclusively expressed in a group or shared between groups, after 72 h and 96 h of biomaterial interaction; (c) Intra-group Venn diagrams showing the total number of proteins identified in macrophage proteome in each group, exclusively expressed after 72 h or 96 h or shared expression at both times of exposure; (d) Pairwise volcano plots (d1–d3) showing differentially expressed proteins (DEPs) between pairwise group comparisons: CoCrErGOHA no wear vs. control (d1) CoCrErGOHA with wear vs. control (d2), CoCrErGOHA with wear vs. CoCrErGOHA no wear (d3); Statistically significant DEPs were computed by Student’s t-test pairwise comparisons with a *p*-value < 0.05.

3.2.1. CoCr Surfaces

Venn diagrams in Figure 2a, b also showed that many proteins were shared between the three groups at 72 h (1182 proteins) and 96 h (953 proteins). Venn diagrams in Figure 2c show a large number of proteins whose expression was maintained at both studied expression

times (72 h and 96 h) for the control group (1638 proteins), CoCr no wear (1097 proteins), and CoCr with wear (950 proteins), indicating high reproducibility of proteomic results for each group when comparing 72 h and 96 h studies.

Differentially expressed proteins (DEPs) between pairwise group comparisons (Figure 2d) revealed that the proteins involved in coagulation and complement systems were significantly upregulated in both CoCr no wear (F2, Serpinc1, A2m in Figure 2d1) and in CoCr with wear (F2, C3, Alb, Apoa1, Itih3, Itih4 in Figure 2d2) vs. the Control group, related to the unspecific adsorption of serum proteins on the surface. It is well-known that plasma proteins are adsorbed on implanted surfaces at the early stages of implantation [20]. Adsorption of albumin (Alb), prothrombin (Serpinc1), alpha-2 macroglobulin (A2m), apolipoprotein A (Apoa1), and complement C3 on CoCr surfaces have already been reported [21], as have inter- α -trypsin inhibitors (Itih3, Itih4) on CoCr particles [22]. Upregulation of coagulation and complement pathways was observed in both CoCr no wear (Supplementary Figure S1e1) and CoCr wear (Supplementary Figure S1e2) vs. the control group. The crosstalk between coagulation and complement cascades is well-known to occur on artificial surfaces [23]. However, the comparison of CoCr wear vs. CoCr no wear (Figure 2d3) reveals that no significant upregulated DEPs belonging to enriched coagulation or complement systems were found (Supplementary Figure S1e3). This suggests that the adsorption of proteins occurs independently of the surface condition [24].

Enzymes involved in the antioxidant system (Gsta3, Gstm1, and Prdx1) are shown to be significantly upregulated in Figure 2d2 and Supplementary Figure S1e2 when comparing CoCr wear vs. the control group. Increased levels of glutathione S-transferase A3 (Gsta3) and glutathione S-transferase Mu 1 (Gstm1), as phase II detoxifying enzymes, revealed increased activity of the glutathione redox system. Upregulation of glutathione system enzymes has been assigned to adaptive responses due to oxidative stress induced by metal exposure [25]. Glutathione S-transferase A3 (Gsta3) and glutathione S-transferase Mu 1 (Gstm1) conjugate glutathione (GSH) with a variety of foreign chemical agents to facilitate their metabolic degradation and excretion [26]. This is the same in the case of toxic heavy metals such as Hg, Pb, Cr, Cd, and As [27], where thiol binding occurs due to the high binding affinity of cysteine sulfhydryl groups in GSH with electrophilic centers of heavy metal ions [26]. Increased protein levels of Gsta3 and Gstm1 could probably indicate an increased metabolism of CoCr by-products by catalyzing the complexation of Cr (III) and Co (II) ions via GSH conjugation. The increased level of peroxiredoxin 1 (Prdx1) observed in CoCr with wear vs. control (Figure 1d2 and Supplementary Figure S1e2) suggests the redox reduction of reactive oxygen species (ROS), as has been observed in cells exposed to metal ions from CoCr alloys [28]. Given that prdx1 has hydrogen peroxide scavenging functions, prdx1 upregulation might confer protection by depleting hydrogen peroxide, thereby, reducing the production of metal-induced ROS. In fact, increased levels of prdx1 have also been observed in cells exposed to metal ions from CoCr alloys [28]. It is known that metallic nanoparticles (NPs) can generate ROS by several reaction mechanisms [29]. This result leads us to think that the NPs that have not been removed and appear accumulated on the worn surfaces after the tribocorrosion tests can induce the identification of ROS in the proteomic profile. In fact, CoCr NPs generate ROS via Cr(III) and Co(II)-induced Fenton reactions, where the Cr and Co ions in lower oxidation states act as catalysts for the conversion of hydrogen peroxide (H₂O₂) into reactive hydroxyl radicals (OH•) [30,31]. When the excessive production of metal-induced ROS cannot be inactivated by the antioxidant systems, oxidative damage usually occurs, such as oxidation of DNA, lipid peroxidation, and/or carbonylation of proteins [32]. Indeed, patients with the highest levels of Cr and Co ions present the highest levels of protein carbonylation [30]. These results suggest Gsta3, Gstm1, and Prdx1 are acting as compensatory mechanisms to enhance the protection against cell damage via the upregulation of redox-homeostasis defense mechanisms in macrophages exposed to worn CoCr.

Enrichment in the detoxification of reactive oxygen species (ROS) was also observed in CoCr wear vs. CoCr no wear (DEP: Hmox1 in Figure 2d3 and Supplementary Figure S1e3),

suggesting that ROS were produced by the interaction with the worn areas. Enrichment analyses revealed the oxidative stress pathway was significantly upregulated (Supplementary Figure S1e3), and its expression is considered an indicator of macrophage oxidative stress induced by metal/metal oxide nanomaterials [33]. Increased levels of Hmox1 have been found in patients with CoCr prosthetic implants [34]. Heme oxygenase 1 (Hmox1) is a well-known antioxidant stress protein whose expression is induced by various stressors such as oxidative stress and heavy metals [35] and its expression is considered a reporter of macrophage oxidative stress induced by metal/metal oxide nanomaterials [33]. In addition, Hmox1 degrades heme into the downstream by-products biliverdin and bilirubin, which are potent direct antioxidants [36], with bilirubin being an inhibitor of protein oxidation in the presence of hydroxyl radicals [37]. All of this suggests that higher levels of Hmox1 could also be a way to protect against oxidative stress caused by CoCr tribocorrosion. In fact, increased mRNA levels of Hmox1 have been found in pseudosynovial tissue removed from CoCr hip arthroplasties that developed adverse reactions to metal debris [34].

Based on the fact that antioxidant system enzymes were upregulated in CoCr wear vs. control (Gsta3, Gstm1, and Prdx1) and CoCr wear vs. CoCr no wear (Hmox), we can assume that worn CoCr surfaces activate the transcription factor Nrf2 in macrophages. Nrf2 is a redox-sensitive transcription factor that directly binds to detoxifying and antioxidant target genes and activates the expression of cytoprotective genes [38] and antioxidant enzymes during mild oxidative stress conditions [39], including the expression of these cytoprotective genes (Gst3, Gstm1, Prdx1, Hmox1) [25,40,41]. Thus, increased Nrf2-mediated expression of redox-regulatory genes has been found in novel macrophage phenotypes found in atherosclerosis lesions, Mhem and Mox, where those phenotypes developed in response to oxidative stress damage [4,35,42]. This macrophage antioxidant phenotype in response to CoCr biomaterial with similar Nrf2-induction of antioxidant genes is likely to act as a compensatory mechanism to prevent the oxidative stress induced by metal ions and/or CoCr particles released upon the eroding process. Macrophages upregulated these antioxidant enzymes to maintain intracellular redox homeostasis to counteract metal-induced oxidative stress, which was likely exacerbated by the degradation phenomena on the CoCr surface.

Additionally, the downregulation of DEPs elucidated molecular mechanism impairments and dysfunctions in macrophages in response to CoCr surfaces. Downregulations of proteins involved in the tricarboxylic acid cycle pathway (TCA) were observed in CoCr with no wear vs. control (Idh3g in Figure 2d1) and CoCr with wear vs. control (Idhg3, Ndufs1 in Supplementary Figure S1e1). Further downregulation of proteins in CoCr with wear vs. control was associated with cellular respiration (Idh3g, Trap1, Cyc1, and Ndufs1 in Figure 2d2 and Supplementary Figure S1e2); respiratory electron transport (Idhg3 and Ndufs1 in Figure 2d2 and Supplementary Figure S1e2); and Acetyl-CoA/Acyl-CoA metabolism pathways (Mvd, Acaa2, and Hmgcs1 in Figure 2d2 and Supplementary Figure S1e2). This indicates dysfunctions in the mitochondrial functions of macrophages exposed to CoCr wear. It was revealed that the effect of wear further exacerbated impairments in cellular respiration when comparing CoCr with wear vs. CoCr no wear (Trap1 in Figure 2d3 and Supplementary Figure S1e3). Impairments in mitochondrial functions can be likely due to the increased presence of remanent metallic debris on the CoCr surfaces in worn areas. Mitochondrial dysfunction due to metal particle exposure has already been described [25], as has the decrease in the TCA metabolic flux on murine macrophages upon exposure to titanium NPs [43], implying that mitochondrial activities were reduced and suggesting the damage to mitochondria after exposure to the CoCr surface.

Recently, downregulation of proteins involved in intra-Golgi traffic and ER to Golgi anterograde transport in CoCr wear vs. control were also downregulated (Napa, Nsf, and Dync1i2 in Figure 2d2, Supplementary Figure S1e2), suggesting impairments in intracellular trafficking. The effect of wear on CoCr seemed to have an impact on intra-Golgi trafficking (Napa and Nsf in Figure 2d3 and Supplementary Figure S1e3). The intracellular trafficking downregulation might be related to ATP depletion. It has been described that

mitochondrial dysfunction induces a decrease in ATP production, which is necessary for correct intracellular trafficking [44]. Mitochondrial dysfunction and an ATP decrease are also reported in macrophages exposed to titanium nanoparticles [43].

3.2.2. CoCrErGO Surfaces

Venn diagrams in Figure 3a,b show that a large number of proteins were expressed in all three groups at 72 h (1148 proteins) and 96 h (1136 proteins). In Figure 3c, each surface maintained a large number of proteins expressed at 72 h and 96 h exposure times (control: 1198 proteins; CoCrErGO no wear: 1261 proteins; and CoCrErGO with wear: 1354 proteins), indicating again the correct reproducibility of proteomic results for these groups when comparing both assayed times.

Differentially expressed proteins between pairwise group comparisons in CoCrErGO no wear vs. control (Figure 3d1) show that some proteins involved in clathrin-mediated endocytosis (CME) were upregulated (PICALM, Arfgap1, and Stam in Figure 3d1), indicating an enhanced cellular uptake of extracellular material via endocytosis. The process of CME was further enriched in CoCrErGO with wear vs. control (PICALM, Eps15, Ap1b1, Ap4s1 in Figure 3d2). PICALM is a core component of clathrin-mediated endocytosis that couples adaptor protein complex 2 (AP-2) with clathrin and has an important role on both surfaces, with and without wear. In fact, other essential proteins enabling the assembly of clathrin coats appeared upregulated upon the wear corrosion process (Eps15 and Ap1b1 in Figure 3d2). Eps15 is a key component required for the initial nucleation step of CME, while Ap1b1 and Ap4s1 belong to the cargo-specific adaptor AP family proteins, linking membrane cargos to clathrin [45]. Upregulation of CME suggests enhanced cellular uptake in macrophages upon the wear corrosion process in comparison with the control group. Tribocorrosion of the CoCrErGO surface results in the detachment of free, desorbed ErGO nanosheets from the surface in addition to CoCr particles. The enhanced pro-inflammatory effect of detached ErGO nanosheets mixed with CoCr particles could be explained by the removal of physically adsorbed ErGO from the CoCr surface, enabling new macrophage-ErGO interactions. The enhancement of cellular uptake via the clathrin-mediated internalization mechanism suggests the engulfment of particles, probably ErGO and CoCr debris, released from the wear corrosion process and accumulated on the surface. It has been shown that the cellular uptake mechanism of GO is mainly influenced by GO lateral size: whereas small GO sheets are internalized by CME, larger sheets are engulfed via phagocytosis [46]. The internalization of particles by CME is size-dependent and limited by the size of CME intracellular vesicles, with a range of 100–500 nm [47]. Consistently, the electrochemically reduced GO sheets deposited on the CoCr surface in this work were previously characterized [48], showing lateral dimensions in the submicron range of 100–1000 nm. Therefore, nano- and submicron ErGO flakes up to 500 nm could be engulfed by CME, while larger ErGO sheets would be internalized via phagocytosis [46,49]. In addition, the increased expression of cargo adaptors Ap1b1 and Ap4s1 might be directly related to the increased biomaterial cargo uptake, since it has been reported that the increased expression of cargo-specific adaptor proteins increases the internalization of their similar receptors and cargo [45].

Moreover, the mechanism of CME might be dependent on or independent of cell-membrane receptors [50]. In our case, the upregulated CME process seems to be dependent on epidermal growth factors, since other proteins that significantly enriched the EGFR1 signaling pathway were upregulated upon the wear corrosion process (Rps6ka1, Stat3, Stat5b, Eps15, and Rps6ka3 in Supplementary Figure S2e2). A wide variety of cell membrane receptors are involved in CME; one of the reported types is the epidermal growth factor receptor [47].

Disagreements in the literature regarding the internalization mechanisms controlling the cellular uptake of carbon-based nanomaterials are found. The visualization of intracellular vesicles by TEM does not provide detailed information regarding the internalization mechanism involved. On the other hand, the use of inhibitors has also been applied to

block the mechanisms of CME and/or phagocytosis individually to study their individual contribution to blocking particle uptake. In the present work, the proteomic analysis provided new insights regarding the molecular mechanisms involved in the internalization of carbon-based nanomaterials (C-BNM), highlighting the relevance of specific proteins involved in CME (Eps15, Ap1b1, Ap4s1, and PICALM).

Cargo-recognition proteins in CME were also upregulated in CoCrErGO with wear in comparison to CoCrErGO with no wear (DEPs: Ap4s1, Cops7a in Figure 3d3), as well as upregulated Eps15, highlighting an enhanced clathrin-endocytic response on macrophages upon the wear corrosion process on CoCrErGO. Increased levels of Stat5b, involved in the EGFR1 signaling cascade, might imply the activation of EGFRs due to clathrin-mediated recognition of ErGO through EGFR receptors [47].

Upregulation of proteins associated with the immune response was observed in CoCrErGO with wear vs. control (Figure 3d2 and Supplementary Figure S2e2), with significant enrichments in Toll-like Receptor 10 (TLR10) and MyD88:MALTIRAP cascades (Rps6ka1, Ikbkg, and Rps6ka3), SUMOylation of immune response proteins (Ikbkg, Ube2i), and interleukin IL-9 and IL-21 signaling (Stat3 and Stat5b). Additional immune-associated proteins (Cnpy4, Chid1) also appeared significantly upregulated in CoCrErGO with wear vs. CoCrErGO no wear (Figure 3d3). Among them, Cnpy4 is known to increase the cell surface expression of TLR4. Based on the proteomic analysis, ErGO nanosheets seem to interact with TLRs in J774A.1 macrophages, activating the TLRs/MyD88/nF-kB signaling cascade. It is known that the canonical nF-KB pathway can be activated by TLRs that are expressed on the cell surface, such as TLR2 and TLR4. Activation of these TLRs triggers the recruitment of the adaptor molecule myeloid differentiation primary-response gene 88 (MyD88), which also requires TIRAP and TRAM for its activation [51]. In the downstream signaling cascade, the NF-kappa-B essential modulator (Ikbkg), also known as NEMO, as part of the IKB Kinase (IKK) complex, allows the translocation of transcription factor nF-kB to the nucleus, constituting an essential component of the nF-kB pathway.

It has already been shown by inhibiting TLR4 and TLR2, MyD88, and nF-kB proteins that the GO-induced secretion of proinflammatory cytokines was reduced in J774 macrophages, showing the crucial roles of those downstream signaling proteins regarding the activation of the nF-kB pathway by exposure to GO [52]. GO-triggered activation of TLR4 and TLR9/MyD88/TRAF6/nF-kB signaling cascades has also been observed in RAW264.7 macrophages [53]. Thus, not only can GO be detected on the cell surface by TLR2/4 but also endosomal GO can be recognized by TLR9 after cellular internalization via endocytosis mechanisms. More recently, microarray transcriptomic analysis of primary human macrophages exposed to single-walled carbon nanotubes (SWCNTs) identified the nF-kB network as an upstream regulator of SWCNT-triggered immune responses [54].

The upregulation of proteins involved in intra-Golgi traffic and Golgi to ER transport also seemed an enriched response both in CoCrErGO no wear vs. control and in CoCrErGO with wear vs. control (Pafah1b3, Stax5a in Figure 3d1,d2), which could suggest enriched intracellular trafficking upon NPs uptake. Besides the generally accepted intracellular trafficking of NPs via the endocytic-lysosomal pathway, it is known that vesicles containing NPs can escape this route and fuse with ER, Golgi, and other organelles via unknown mechanisms [50].

Downregulation of proteins involved in the electron transport chain was observed both in CoCrErGO with no wear vs. control (Por, Cdk1 in Figure 3d1) and in CoCrErGO with wear vs. control (Por, Ppif in Figure 3d2), suggesting mitochondrial dysfunctions in macrophages upon exposure to ErGO. It has been widely reported that the impact of GO in mitochondria is caused by perturbations in mitochondrial structure and functions, such as the decrease in mitochondrial membrane potentials, disturbances in the electron transport chain, dysregulation of mitochondrial Ca²⁺ homeostasis, inhibited or impaired ATP synthesis, and downregulation in the expression of proteins of the TCA cycle pathway and mitochondrial electron transfer chain complexes [55–57], while pristine graphene [58] and MWCNT [59] also induce similar detrimental effects in mitochondria.

The downregulation of proteins involved in autophagy in CoCrErGO with wear vs. control (Eif2s1, Mapk1 in Figure 3d2) suggested an impaired autophagic response due to the enhanced cellular uptake of ErGO NPs deposited on CoCrErGO surfaces after wear corrosion tests. After microparticles and NPs are internalized by the cells, they can travel to a wide variety of subcellular locations and may have more than one final intracellular fate [50]. However, there is strong evidence that lysosomes are the main subcellular location of NPs aggregation, including the accumulation of metallic NPs and C-BNMs [44]. An impaired degradative capacity of lysosomes has been described when GO nanosheets are accumulated inside these organelles, in turn blocking the normal progression of the autophagic flux and limiting the clearance of autophagosomes both in human [35] and rat neural cells [44] as well as mouse macrophages [44]. Therefore, the main downregulation of Eif2s1 and, to a lesser extent, the downregulation of Mapk1 are probably evidencing the autophagic blockage in macrophages exposed to worn CoCrErGO vs. the control group.

3.2.3. CoCrErGOHA Surfaces

The Venn diagrams of CoCrErGOHA in Figure 4 show that a smaller number of proteins were expressed in all three groups at 72 h (685 ID proteins), while the number of shared expressed proteins almost doubled at 96 h (1019 ID proteins). Venn diagrams in Figure 4c show the numbers of proteins whose expression was maintained in the control group (1446 proteins), in CoCrErGOHA with no wear (987 proteins), and in CoCrErGOHA with wear (550 proteins) at both times of exposure (72 h and 96 h).

Differentially expressed proteins (DEPs) between pairwise group comparisons showed that while few upregulated DEPs appeared in CoCrErGOHA surfaces compared with controls (16 and 12 upregulated DEPs in Figure 4d1,d2, respectively), no upregulated DEPs appeared associated with the wear corrosion of this surface (Figure 4d3). Upregulation of inter- α -trypsin inhibitor heavy chain 2 protein in both surfaces, CoCrErGOHA no wear and CoCrErGOHA with wear vs. control (Itih2 in Figure 4d1,d2) might be specific to the HA modification of the surface since it is known that this protein forms complexes with hyaluronan [60,61]. Upregulation of autophagy in mitochondria in CoCrErGOHA vs. control (Sqstm1 and Cisd2 in Figure 4d1,e1) might be a mechanism to counteract the damage to these cellular organelles, promoting the cleansing of damaged mitochondria via autophagy. Protection of mitochondrial function by hyaluronic acid in HA-coated NPs by mitophagy has already been reported [55,62]. After subjecting the surface to the wear corrosion process, some deposition of serum proteins occurred in CoCrErGOHA with wear vs. control (F2 in Figure 4d2,e2), suggesting the unspecific adsorption of this coagulation protein upon subjecting the surface to wear.

Moreover, a pattern in the reduction of upregulations was observed. This is while downregulated DEPs became predominant in CoCrErGOHA with wear vs. control (46 downregulated DEPs in Figure 4d2), and only downregulations appeared in CoCrErGOHA with wear vs. CoCrErGOHA with no wear (26 downregulated DEPs in Figure 4d3). This suggests that the main actions of these surfaces are the suppression or inhibition of molecular mechanisms/pathways. Gene ontology enrichment analyses significantly indicated downregulated TNF- α nF-kB pathway (Psm13, Psm7, Cul1 in Figure 4d2 and Supplementary Figure S3e2), IL-1 signaling (Cul1, Mapk1, Sqstm1 in Figure 4d2 and Supplementary Figure S3e2), IL-17 signaling (Mapk1, Cul1 in Figure 4d2 and Supplementary Figure S3e2) and downregulated innate immune system (Ap1m1, Ncstn, Ostf1, Psm13, Dhx36, Cul1, Dync1li1, Psm7, Atp6v1a, Mapk1 in Figure 4d2 and Supplementary Figure S3e2) in CoCrErGOHA with wear vs. control. This suggests the attenuation of pro-inflammatory signals by the effect of HA functionalization.

The absence of upregulation of the TLR-nF-kB pathway in volcano plots (Figure 4d1–d3), which was observed upregulated in the previous surface without HA functionalization (surface CoCrErGO, Figure 3d2,d3), may suggest that upon HA functionalization on the CoCrErGOHA surface, coating of ErGO sheets with HA may cause the escape of ErGO from binding to TLRs. It has been widely reported that high molecular weight (HMW)

HA can suppress IL-1b levels, decrease the IL-1-dependent expression of metalloproteinases, or decrease the nF-kB expression and synthesis, i.e., reduce the transcription of pro-inflammatory cytokines and chemokines [63–65]. The anti-inflammatory role of HMW-HA has been widely exploited to develop HA-based commercial products for the treatment of inflammatory diseases such as osteoarthritis or intestinal inflammation [63]. Importantly, the molecular mass of HA strongly determines the inflammatory response. Low molecular weight (LMW)-HA (<500 kDa) induces a pro-inflammatory response of macrophages, which are polarized towards the M1 phenotype, whereas high molecular weight (HMW)-HA (>500 kDa) induces an anti-inflammatory effect with macrophage polarization towards the alternative M2 phenotype [66]. In this work, the induction of an anti-inflammatory response was desired. Hence, HMW-HA (1500–1800 kDa) was used for functionalization. Significant downregulation of the TNF- α nF-kB pathway (Psm13, Psm17, and Cul1 in Figure 4d2 and Supplementary Figure S3e2) and significant downregulation of pro-inflammatory IL-1 and IL-17 signaling pathways (Mapk1 and Cul1 in Figure 4d2 and Supplementary Figure S3e2) in CoCrErGOHA with wear vs. control may indicate a polarization shift from the M1 to the M2 phenotype by inhibition of M1-related pathways. The Notch signaling pathway was also significantly downregulated in both CoCrErGOHA no wear vs. control (Ncstn in Figure 4d1 and Supplementary Figure S3e1) and CoCrErGOHA wear vs. control (Ncstn, Cul1, and Mapk1 in Figure 4d2 and Supplementary Figure S3e2). The activation of the Notch pathway represents a mechanism to reprogram mitochondrial metabolism in favor of glycolysis, contributing to mitochondrial M1 genes [4]. In accordance with downregulated Notch signaling, the TCA cycle was downregulated both in CoCrErGOHA no wear (Sdhb in Figure 4d1 and Supplementary Figure S3e1) as well as in CoCrErGOHA with wear (Dlat, Idh2 in Figure 4d2 and Supplementary Figure S3e2) vs. controls. This further suggests the downregulation of the Notch/TCA cycle signaling pathway in macrophages exposed to CoCrErGOHA surfaces. It has also been reported that inhibition of the Notch pathway diminished macrophage M1 activation [67]. Therefore, downregulation of the TNF- α nF-kB pathway, IL-1 and IL-17, and Notch pathways in macrophages exposed to CoCrErGOHA surfaces attenuated the expression of M1 genes and thus the pro-inflammatory response (see also Section 3.5). The immunosuppressive effects of HMW-HA were enhanced on the surface subjected to degradation phenomena, which could be explained by the detachment of HA polymeric strands from the functionalized surface upon tribocorrosion. This allows a larger number of interactions between HMW-HA and macrophages.

Despite the improved anti-inflammatory responses, some impairments in mitochondrial activities are still observed in the presence of CoCrErGOHA surfaces, as evidenced by downregulation in the respirasome and electron transfer activity (Sdhb, Cyts in Figure 4d1 and Supplementary Figure S3e1) in CoCrErGOHA no wear vs. control. Downregulated cellular respiration (Dlat, Slc25a12, Mybbp1a, and Idh2 in Figure 4d2 and Supplementary Figure S3e2) was observed in CoCrErGOHA with wear vs. control. Tribocorrosion on this surface also seemed to influence mitochondrial dysfunction due to downregulation of the NAD metabolic process (Dlat, Slc25a12 in Figure 4d3 and Supplementary Figure S3e3), probably again due to the release of higher amounts of biomaterial particles upon the wear corrosion process, affecting the mitochondrial compartment.

3.3. Effect of HA Surface Functionalization on TNF- α Levels

Previous studies in the functionalization of CoCrErGO surfaces with HA provided evidence of an improvement in the inflammatory response of J744A.1 macrophages [11]. Increased TNF- α levels after exposure to CoCrErGO for 72 h were attributed to ErGO interactions with TLRs in cells, which activated the nF-kB pathway and the subsequent production of pro-inflammatory cytokines such as TNF- α . This is while HA functionalization constituted a suitable hydrophilic material to avoid the inflammatory response [11]. Hence, in this work, the effect of surface modification on inflammatory response was evaluated at a longer exposure time to know if the observed behavior was maintained over time. Table 1

shows the level of pro-inflammatory cytokine TNF- α , evaluated in J744A.1 macrophages' supernatants after being cultured for 72 and 96 h on CoCrErGO and CoCrErGOHA surfaces. Regardless of the surface condition, TNF- α levels increased for control M0 macrophages, revealing the pro-inflammatory response of macrophages when they are exposed to the biomaterial surfaces. The increase in pro-inflammatory response was exacerbated when exposing macrophages to the CoCrErGO surface, in agreement with proteomic results in Section 3.2, where upregulated DEPs significantly enriched the TLRs-MyD88-nF-kB pathway. However, it should be highlighted that this pro-inflammatory response was more modest once the functionalization of CoCrErGO with HA was performed, both after exposing the macrophages at 72 h and 96 h to CoCrErGOHA surfaces. Herein, assessment of TNF- α levels revealed the attenuation of the pro-inflammatory response after functionalization of CoCrErGO with HA, which was maintained both at 72 h and at a longer time of 96 h.

Table 1. Secreted TNF- α levels (pg/mL) of J744A.1 macrophages in response to the modified surfaces CoCrErGO and CoCrErGOHA for 72 h and 96 h. Control J744A.1 macrophages (M0) are added for comparative purposes.

Time of Exposure	Control	CoCrErGO No Wear	CoCrErGOHA No Wear
72 h	183.52	1358.06	1063.88
96 h	388.42	2465.38	949.09

3.4. Inflammatory Balance (TNF- α /IL-10 Ratios)

The quantification of specific markers of opposite phenotypes at each extreme of the polarization spectrum, i.e., M1 and M2, simplifies the assignment of intermediate macrophage states across the broad polarization spectrum. The ratio between pro-inflammatory TNF- α and anti-inflammatory IL-10 provides a measurable value about macrophages polarized towards the M1 phenotype vs. the M2 phenotype.

Table 2 shows the M1/M2 ratio estimated in the ratio between the secreted TNF- α and IL-10 concentrations from supernatants of J744A.1 macrophages were seeded on each modified surface, before and after wear corrosion tests, both at 72 h and 96 h, respectively.

Table 2. TNF- α /IL-10 ratios of J744A.1 macrophage supernatants after being exposed for 72 h and 96 h to surfaces CoCr, CoCrErGO, and CoCrErGOHA without application of wear corrosion tests (i.e., “no wear”) and to surfaces subjected to wear corrosion processes (i.e., “with wear”).

TNF- α /IL-10 (72 h)	CoCr	TNF- α /IL-10 (96 h)	CoCrErGO	CoCrErGOHA
control	1.60	control	1.90	1.55
no wear	27.34	no wear	13.27	9.78
with wear	82.76	with wear	24.79	20.41

3.4.1. Effect of Surface Modification

Regarding the effect of intact surfaces without wear corrosion, macrophage exposure to any surface triggered an increase in TNF- α /IL-10 ratios with respect to non-polarized macrophages (control group M0 in Table 2), implying that macrophages were polarized towards M1 in response to any biomaterial surfaces. The highest TNF- α /IL-10 ratio was achieved in response to the CoCr surface. This inflammatory response was observed together with increased adsorption of serum proteins on this surface (see Section 3.2, Supplementary Figure S1e1). The adsorption of alpha2 macroglobulin (A2M) probably contributed to the increased M1/M2 ratio by leading to TNF- α production in macrophages. Increased adsorption of A2M on biomaterial surfaces has been associated with increased TNF- α release due to cells' interaction via the A2M receptor in monocytes [68], indicating

that the observed upregulation of adsorbed proteins on the CoCr surface plays an important role in the macrophage inflammation response.

Upon surface modification with ErGO (Table 2), TNF- α /IL-10 ratios decreased in CoCrErGO (ratio around 13) vs. CoCr (ratio around 27), which can be directly related to the decreased protein adsorption in CoCrErGO (see Section 3.3, Supplementary Figure S2e1), where previous upregulation of plasma proteins detected on CoCr was not observed upon ErGO surface modification. Decreased TNF- α and increased IL-10 cytokine secretions have been directly attributed to the precise control of protein adsorption, modulating macrophage interaction with the biomaterial [6]. Inhibition of protein adsorption on the CoCrErGO surface was likely mediated by the anti-fouling properties of ErGO, originating from the anti-fouling properties of pristine graphene [69]. Graphene in its oxidized form as graphene oxide is also proven to inhibit the adsorption of proteins in fouling models using bovine serum albumin [70–72], where the addition of GO increased the fouling resistance of the materials.

Following HA surface functionalization, the CoCrErGOHA surface provided the lowest TNF- α /IL-10 ratio among the three different surfaces, revealing that HA functionalization further attenuated the classically activated M1 macrophage response observed on the bare CoCr surface. M1 attenuation correlates with proteomic analysis, where down-regulation of the Notch pathway in the macrophage proteome profile was observed in response to this surface (see Section 3.4, Supplementary Figure S3e1). The Notch pathway promotes the activation of M1 macrophages [4], while its inhibition raises the secretion of IL-10 [73]. Inhibition of pro-inflammatory signals by HMW-HA, which confers some of its well-known anti-inflammatory properties, is exploited for the treatment of a variety of inflammatory conditions [63]. Therefore, HA surface functionalization triggered the attenuation of the M1 phenotype while encouraging the transition to the M2 phenotype in macrophages exposed to the surface modification CoCrErGOHA.

3.4.2. Effect of Wear on Inflammatory Balance

The effect of wear corrosion on all surfaces triggered an increase in TNF- α /IL-10 ratios (Table 2), i.e., exacerbated the macrophage polarization towards the M1 phenotype, highlighting a pro-inflammatory response.

A drastic M1 additional polarization was observed in the CoCr surface subjected to the wear corrosion process (TNF- α /IL-10 ratio around 83). The exacerbation of the inflammatory response was observed together with the upregulation of proteins involved in platelet activation, coagulation cascades, complement activation, detoxification of ROS, and oxidative stress on the CoCr surface (see Section 3.2, Supplementary Figure S1e2, and Supplementary Figure S1e3). Increased adsorption of complement proteins on biomaterial surfaces induces macrophage polarization towards the inflammatory M1 phenotype [74], where the adsorbed complement proteins on the biomaterial surface interact with macrophage complement cell receptors, modulating cytokine production [75]. It is known that biomaterial-induced inflammation is largely driven by complement activation [76], which is dependent on TNF- α release [77]. The increased adsorption of complement proteins on biomaterial surfaces also results in pro-inflammatory macrophage polarization [74]. Thus, the TNF- α /IL-10 ratio correlates with proteomic results, revealing a mechanism involved regarding the exacerbation of M1 polarization and acute inflammation in response to the CoCr surface after applying the wear corrosion process.

Nevertheless, a 3-fold increase in the TNF- α /IL-10 ratio upon tribocorrosion of CoCr suggests that other pro-inflammatory parameters, besides the action of complement proteins and other adsorbed plasma proteins, may be contributing to the M1 activation. Likely, tribocorrosion-induced ROS was also a determining factor for the observed increase in M1/M2 ratio, revealing the pro-oxidant effect of the wear corrosion phenomenon on the CoCr surface. Importantly, ROS can induce the production of TNF- α . ROS activates MAPK, an oxidation-reduction sensitive signaling pathway, which in turn can activate nF- κ B signaling downstream, promoting transcription of TNF- α [78]. It is also known

that the ROS species hydrogen peroxide induces M1 polarization in macrophages via the ROS-MAPK-NF κ B-P65 signaling pathway [79].

A more moderate M1 polarization occurred on the CoCrErGO surface when the surface was subjected to wear corrosion phenomena. The additional M1 polarization occurring on the CoCrErGO surface after wear corrosion phenomena (TNF- α /IL-10 ratio around 25) was moderate vs. no wear on CoCrErGO surfaces (TNF- α /IL-10 ratio 13), inferring a modest tribocorrosion-induced inflammation response. Upregulation of proteins involved in the TLRs/MyD88/nF-kB signaling cascade (see Section 3.2.2, Supplementary Figure S2e2), due to interaction of ErGO nanosheets with TLR receptors activating the nF-kB pathway, further promotes the transcription of pro-inflammatory genes such as TNF- α and contributes to M1 polarization [80], thus correlating with the moderate increase in the TNF- α /IL-10 ratio (Table 2). Enhanced production of TNF- α has also been reported both in J774 [52] and RAW264.7 [53] macrophages in response to GO, where the activated signaling cascades also operated through the nF-kB canonical pathway via TLR2 and TLR4/MyD88/nF-kB signaling in J774 or TLR4 and TLR9/MyD88/TRAF6-nF-kB in RAW264.7. Hence, activations in the nF-kB signaling cascade observed by increased expression of proteins in proteomics analysis (Ikbkg, Rps6ka1, Rps6ka3) were observed together with the cytokine expression downstream of NF-kB signaling by a moderate M1 polarization in TNF- α /IL-10 ratios (Table 2) in macrophages exposed to worn CoCrErGO.

Regarding the CoCrErGOHA surface, the contribution of the wear corrosion of this surface to M1 polarization was also moderate (TNF- α /IL-10 ratio around 20) in comparison with the intact surface (TNF- α /IL-10 ratio around 10), which was observed together with upregulation of prothrombin (F2) by proteomic analysis that suggests that it could be associated with the additional M1 polarity [81]. Nevertheless, the observed TNF- α /IL-10 ratio from macrophages exposed to worn CoCrErGOHA surfaces was the lowest among the three surfaces with wear, suggesting a shift from acute to mild inflammation upon degrading the surface when HMW-HA functionalization was present. M1 attenuation in the CoCrErGOHA surface was observed together with the observed downregulation of pathways associated with M1 activation in the proteomics section (downregulation of the nF-kB pathway, the IL-1 and IL-17 signaling pathway, and the NOTCH pathway) (see Section 3.2.3, Supplementary Figure S3e2).

Molecular mechanisms of attenuation of pro-inflammatory signals by HMW-HA have been proposed, mainly consisting of a shielding effect of HMW-HA when binding to its several receptors, such as CD44 on the plasma membrane [82], which prevents the activation of cascades signaled by inflammatory cytokines such as IFN α , TNF- α , and IL1 β via impeding the contact with their receptors. After wear corrosion, these results revealed the anti-inflammatory role of HMW-HA, probably due to the role of desorbed HMW-HA strands, which are detached from the CoCrErGOHA surface upon tribocorrosion and may provide enhanced anti-inflammatory effects on J774A.1 macrophages. This revealed that immunomodulation of the macrophage response by the surface CoCrErGOHA was preserved even when the surface was subjected to wear corrosion.

In fact, besides the anti-inflammatory properties of HMW-HA, the anti-oxidative and anti-apoptotic effects of HMW-HA have been widely observed. HMW-HA has been previously shown to protect cells from oxidative stress induced by ROS or toxic chemical substances [83–85], including exposure to Cr(VI) [86]. The cytoprotective effects of HA also depend on its size, and very high molecular weight HA (vHMW-HA) has superior cytoprotective properties than HMW-HA because it interacts differently with the CD44 receptor, leading to distinct transcriptional changes [87,88]. When considering the degradation of biomaterials or nanoparticles, it has been observed that HMW-HA decreased the oxidative potential of fine particulate matter (PM) by repressing the ROS generation stimulated by PM_{2.5} (PM_{2.5}, aerodynamic diameter <2.5 μ m), decreasing the oxidative potential of PM_{2.5} by downregulating the oxidative stress level and inhibiting the activation of ROS-induced signaling pathways, leading to decreased TNF- α levels as well [89]. Thus, HMW-HA might

also confer anti-oxidative protection upon wear corrosion of the CoCrErGOHA surface, with the subsequent generation of degradation products such as particulate debris.

3.5. Effects on Osteoblast Response of Macrophages Supernatants Collected after Exposure to Material

To understand the cellular reactions to implanted materials, it is necessary to study the consequences of macrophages' response to osteoblast metabolism because macrophages are in close contact with osteoblasts. With this objective, macrophage supernatants exposed to materials before and after wear were evaluated on osteoblast cultures to study the effects on metabolic activity (WST-1 assay), plasma membrane damage (LDH assay) [18], and phosphatase alkaline activity.

The total number of pre-osteoblastic cells, estimated by total LDH content, has not presented statistically significant differences between any of the supernatants tested, indicating that the treatments did not have any effect on cell proliferation. Additionally, macrophage supernatants from 72 and 96-h cultures showed cytotoxicity on osteoblast cultures below 30% (data not shown), which is considered a negligible cytotoxic effect by ISO Standards. Furthermore, the osteoblasts' morphology was normal, comparable to the control (no material), for all the samples tested.

The pre-osteoblast response towards macrophage supernatants was analyzed by the WST-1 assay (Figure 5). Supernatants from controls (absence of material) incubated for 72 and 96 h with macrophages did not show statistically significant differences with respect to the response induced by fresh cell culture medium (complete DMEM). In the case of supernatants exposed to CoCr before wear-assay, both at 72 and 96 h, the WST-1 value has not shown differences with the control or complete DMEM. The presence of ErGO on the CoCr surface induced a higher response of WST-1 in pre-osteoblast cells with the 96-h-exposed supernatant. Additional surface modification by HA (CoCrErGOHA) did not induce an increase in the WST-1 response for 72 or 96 h supernatants referred to as control, indeed preventing the increase provoked by ErGO at 96 h.

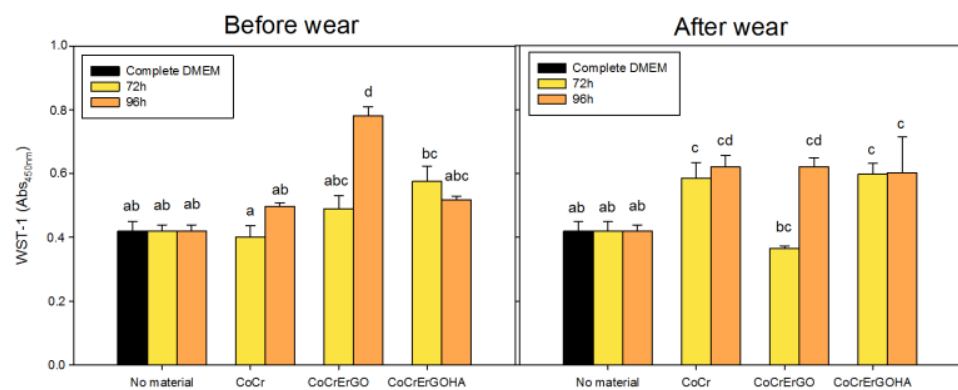


Figure 5. WST-1 assay revealed an increased response of pre-osteoblasts against the supernatant from the CoCr after the wear assay (72 and 96 h) and ErGO before the wear assay (96 h). The profile of response toward ErGOHA has not shown significant differences with CoCr. The results are expressed as $\bar{x} \pm SD$. Samples sharing identical letters do not have statistically significant differences with $p < 0.01$.

Macrophage supernatants exposed to worn materials were also analyzed to study the consequences on osteoblast response induced by wear. As Figure 5 shows, the supernatants of worn CoCr, both at 72 and 96 h, raised the WST-1 value of pre-osteoblasts. CoCrErGO supernatants of 72 h showed that ErGO prevented the response observed in worn CoCr, but it was not maintained by the 96 h supernatant. The adsorption of ErGO to CoCr was able to inhibit the raising of the WST-1 response obtained with worn CoCr at 72 h but not at a longer exposure time. Supernatants of worn CoCrErGOHA surfaces, at both 72 and 96 h, showed an increase in respiratory activity over their control, like that observed in

worn CoCr samples. On the other hand, the adsorption of HA over ErGO hampered the effect produced by ErGO at 96 h, but it did not show any influence on the wear process, as it produced similar results to those detected for CoCr with and without wear.

Although in the WST-1 assay, the amount of produced formazan dye is usually considered indicative of the metabolic activity of cells, the profile of the WST-1 response of pre-osteoblasts against macrophage supernatants seems to be associated with inflammatory parameters. The increase in WST-1 value provoked by worn CoCr at 72 and 96 h of exposure is not the consequence of a higher number of cells, as demonstrated by total LDH measurements. This behavior could be associated with the highest value of the ratio $\text{TNF-}\alpha/\text{IL-10}$ found for worn CoCr (Table 2). The inflammatory stimulus induced by macrophage supernatants may produce an enhancement of the superoxide anion (a free radical that may induce lipid peroxidation and protein and DNA damage) in pre-osteoblasts, which may interfere with the WST-1 reaction, causing an increase in response. There are many reports about the ability of the superoxide anion to reduce WST-1 to formazan [90,91]. Accordingly, Hameister et al. [92] reported that macrophages displayed strong $\text{TNF-}\alpha$ immune expression in periprosthetic tissues containing metal wear debris. The authors attributed the mentioned effect to Co^{2+} released from this kind of material. $\text{TNF-}\alpha$, in turn, induced inflammation involving reactive oxygen species in human osteoblast-like cells [93]. Jonitz-Heincke et al. [93] found a similar effect caused by Co^{2+} on pre-osteoblast cells where the cell number remained stable although an increase in WST-1 value was detectable in a wide range of concentrations. This phenomenon was not observed for Cr^{3+} salts or CoCr-based particles [93]. The authors attribute these results to Co^{2+} 's ability to enter the cell through the Ca^{2+} transport system, triggering hypoxia-like reactions that enhance glycolytic reactions. However, they did not dismiss the fact that the results of metabolic activity can reflect the presence of superoxide, which is associated with phagocytosis and oxidative burst. Hence, the results described here enabled us to confirm that worn CoCr surfaces induced a release of pro-inflammatory cytokines by macrophages towards supernatants that might provoke the increase in the WST-1 value on pre-osteoblasts, presumably mediated by superoxide.

On the other hand, the presence of Cr^{3+} and/or Co^{2+} ions, or fragmented ErGO, in macrophage supernatants should also be considered as a possible reason for the direct induction of superoxide in pre-osteoblasts [94,95]. It is also possible that supernatants containing the ions Co^{2+} , Cr^{3+} , or fragmented ErGO can directly interfere with the WST-1 response since several previous reports pointed out misleading results obtained from WST-1 assays. Some reducing reagents (such as mercaptoethanol, L-cysteine, or L-ascorbic acid) can replace the mitochondrial hydrogenase activity, producing formazan from tetrazolium salts, giving falsely augmented responses [96]. Additionally, carbon nanotubes, carbon black, nanoparticles, and degradation products of Mg and Mn can interfere with the reduction of WST-1 to formazan, suggesting false cytotoxicity results [97].

In the same way of analysis, the highest level of $\text{TNF-}\alpha$ detected in macrophage supernatants exposed to CoCrErGO without wear for 96 h (Table 1) could explain the higher WST-1 value measured in pre-osteoblast culture. The presence of HA improved the performance of the CoCrErGO material without wear after 96 h, lowering the WST-1 response. This result is in agreement with a lesser value of $\text{TNF-}\alpha$ (Table 1) and a lower $\text{TNF-}\alpha/\text{IL-10}$ ratio (Table 2) in the macrophage supernatant of CoCrErGOHA compared with CoCrErGO.

It was also interesting to measure the effect of these macrophage supernatants on the phosphatase alkaline (ALP) activity in pre-osteoblasts. ALP is an enzyme that plays a role in the mineralization of bone. Given this, it is important for the correct osseointegration and attachment of implants to bone. It is worth highlighting the fact that the macrophage supernatants of 72 and 96 h from worn CoCr produced an inhibition in differentiation (a decrease in ALP expression) (Figure 6). This result is in agreement with other authors who have reported similar effects caused by Co^{2+} ions and CoCr-based particles [93]. This evidence supports the hypothesis that released ions have an important role in the biological

responses of pre-osteoblasts to macrophage supernatants. The presence of ErGO on the CoCr surface avoids the ALP inhibition caused by worn CoCr, which gave ALP levels comparable to control values at 72 and 96 h. In the case of the supernatants of worn CoCrErGOHA, HA adsorption not only reversed the inhibition observed by worn CoCr but there even was an induction of ALP activity relative to its control at 96 h.

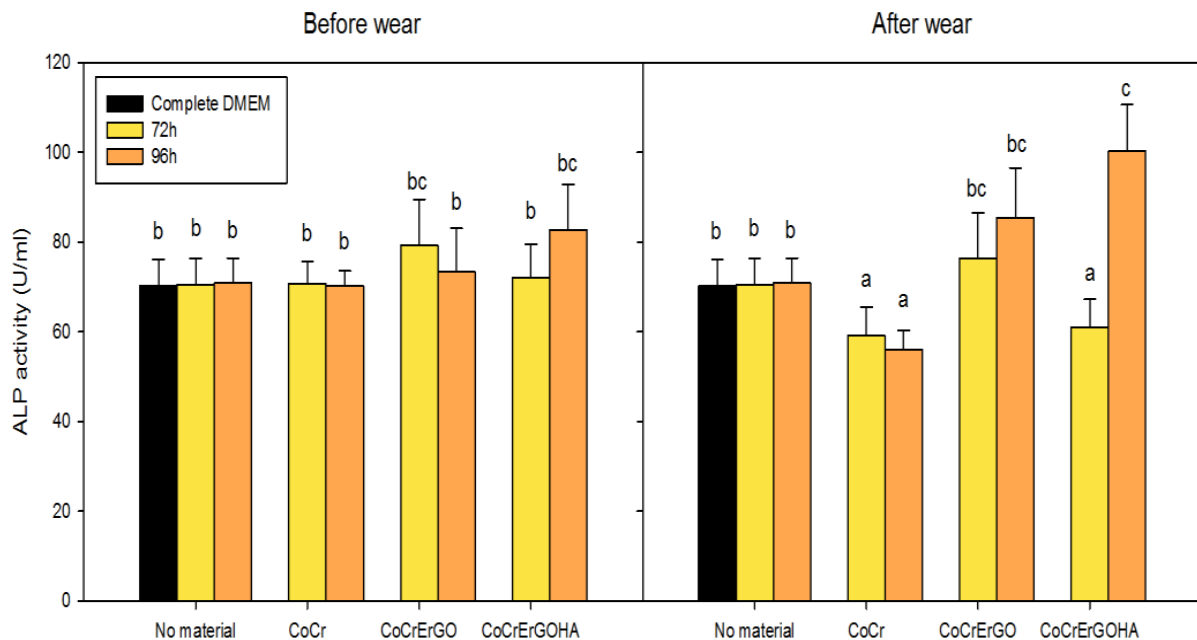


Figure 6. The effect of macrophage supernatants on ALP activity in pre-osteoblast MC3T3E-1. The cells were incubated with an osteogenic medium for 10 days and an additional 24 h with macrophage supernatants. CoCr after wear-assay caused inhibition in ALP activity that was reverted by ErGO and ErGOHA. The results are expressed as $\bar{x} \pm SD$. Samples sharing identical letters do not have statistically significant differences with a $p < 0.01$.

Results on cytotoxicity (LDH assay) and ALP activity in osteoblast cultures allow us to consider that the adsorption of HA on CoCrErGO surfaces would be a recommended surface treatment since macrophages exposed to it would induce the maturation of pre-osteoblasts into osteoblasts, promoting the mineralization processes necessary for bone repair. Instead, CoCr and CoCrErGO provoked an increase in the WST-1 response in pre-osteoblasts, presumably associated with the superoxide production elicited by an inflammatory signal from macrophages. Evidence reported in the literature supports the role of Co^{2+} in triggering this effect. Moreover, CoCr produced an inhibition of ALP activity that was compensated by ErGO and ErGOHA, being even higher than control in the latter case when HA functionalization was present.

4. Conclusions

The use of combinatory analysis in proteomics and inflammatory studies provided relationships between the observed macrophage polarities and the molecular mechanisms involved in the response to material surfaces. The ErGO coating on CoCr surfaces decreased the unspecific binding of plasma proteins, which correlated with the decrease in M1 polarization of macrophages, which is also evidenced on CoCrErGOHA surfaces. However, the CoCr surfaces induced the largest M1 polarization due to the increased adsorption of plasma proteins involved in complement and coagulation cascades, contributing to the inflammation response.

The wear corrosion process of ErGO-modified surfaces enhanced the clathrin-mediated endocytosis response on the macrophages, indicating the cellular internalization of ErGO nanosheets via this uptake mechanism. The mechanisms involved could be related to the

pro-inflammatory effect of detached ErGO nanosheets upon degradation phenomena of the CoCrErGO surface. The anti-inflammatory contribution of worn CoCrErGOHA surfaces was confirmed both by proteomic analyses and the M1/M2 polarization ratio in J774.A1 macrophages, further highlighting the anti-inflammatory effects. However, the wear corrosion process of the CoCr surface promoted acute inflammation by an exacerbated M1 polarization, together with a macrophage antioxidant phenotype due to the upregulation of REDOX mechanisms.

The ALP activity in osteoblast cultures induced by macrophage supernatants makes it possible to consider that the adsorption of HA on the surface would be a recommended surface treatment since it would induce the maturation of pre-osteoblasts into mature osteoblasts, therefore promoting the mineralization processes necessary for bone repair.

Supplementary Materials: The following supporting information can be downloaded at: <https://www.mdpi.com/article/10.3390/met13030598/s1>, Figure S1: Pairwise Gene-Ontology enrichment analyses in response to CoCr surfaces. Figure S2: Pairwise Gene-Ontology enrichment analyses in response to CoCrErGO surfaces.; Figure S3: Pairwise Gene-Ontology enrichment analyses in response to CoCrErGOHA surfaces.

Author Contributions: Conceptualization, L.S.-L., B.C., N.S.F., M.L.E., M.C.G.-A. and R.M.L.; methodology, L.S.-L., N.R.d.T., V.d.I.R., B.C., N.S.F., M.L.E., M.C.G.-A. and R.M.L.; software, L.S.-L., N.R.d.T., V.d.I.R., N.S.F., B.C., M.L.E., M.C.G.-A. and R.M.L.; validation, L.S.-L., N.R.d.T., V.d.I.R., N.S.F., B.C., M.L.E., M.C.G.-A. and R.M.L.; formal analysis, L.S.-L., N.R.d.T., V.d.I.R., N.S.F., B.C., M.L.E., M.C.G.-A. and R.M.L.; investigation, L.S.-L., B.C., N.S.F., M.L.E., M.C.G.-A. and R.M.L.; resources, M.L.E., M.C.G.-A. and R.M.L.; data curation, L.S.-L., N.R.d.T., V.d.I.R., N.S.F., B.C., M.L.E., M.C.G.-A. and R.M.L.; writing—original draft preparation, L.S.-L., B.C., N.S.F., M.L.E., M.C.G.-A. and R.M.L.; writing—review and editing, L.S.-L., V.d.I.R., N.S.F., B.C., M.L.E., M.C.G.-A. and R.M.L.; visualization, L.S.-L., N.R.d.T., V.d.I.R., N.S.F., B.C., M.L.E., M.C.G.-A. and R.M.L.; supervision, B.C., M.L.E., M.C.G.-A. and R.M.L.; project administration, M.L.E., M.C.G.-A. and R.M.L.; funding acquisition, M.L.E., M.C.G.-A. and R.M.L. All authors have read and agreed to the published version of the manuscript.

Funding: Financial support was received through the RTI2018-101506-B-C31 and RTI2018-101506-B-C33 from the Ministerio de Ciencia, Innovación y Universidades (MICIU/FEDER) in Spain. L. Sánchez-López thanks financial support from MICIU for the predoctoral contract PRE2019-090122. ANPCyT (PICT 2019-0631), CONICET (PIP 112-201501-00601CO and External Grant for Young Researchers for N.S.F.) and UNLP (11/X900).

Data Availability Statement: Data availability were not already share due to privacy restrictions. In the future, data will be deposited in the institutional repository of CSIC (Digital CSIC, <https://digital.csic.es>).

Acknowledgments: The authors wish to thank Francisco García Tabares (F.G.T.) and Tamar San Hipólito Marín (T.S.H.M.) of the Proteomic and genomic facility at the Centro de Investigaciones Biológicas, CIB-CSIC, for technical assistance in the preparation of samples for proteomic analysis. N.S.F. thanks CONICET for an external grant for young researchers and ANPCyT for financial support (Proyecto PICT 2019-00631).

Conflicts of Interest: There are no conflicts of interest to declare. The authors will receive no benefit of any kind, either directly or indirectly.

References

1. Saleh, L.S.; Bryant, S.J. In vitro and in vivo models for assessing the host response to biomaterials. *Drug Discov. Today Dis. Models* **2017**, *24*, 13–21. [[CrossRef](#)] [[PubMed](#)]
2. Martin, K.E.; García, A.J. Macrophage phenotypes in tissue repair and the foreign body response: Implications for biomaterial-based regenerative medicine strategies. *Acta Biomater.* **2021**, *133*, 4–16. [[CrossRef](#)] [[PubMed](#)]
3. Barbosa, J.N.; Vasconcelos, D.P. Macrophage response to biomaterials. In *Handbook of Biomaterials Biocompatibility*; Elsevier: Cambridge, MA, USA, 2020; pp. 43–52. [[CrossRef](#)]
4. Sottero, B.; Testa, G.; Gamba, P.; Staurengi, E.; Giannelli, S.; Leonarduzzi, G. Macrophage polarization by potential nutraceutical compounds: A strategic approach to counteract inflammation in atherosclerosis. *Free Radic. Biol. Med.* **2022**, *181*, 251–269. [[CrossRef](#)] [[PubMed](#)]

5. Mantovani, A.; Biswas, S.; Galdiero, M.; Sica, A.; Locati, M. Macrophage plasticity and polarization in tissue repair and remodelling: Macrophage plasticity and polarization in tissue repair and remodelling. *J. Pathol.* **2013**, *229*, 176–185. [[CrossRef](#)] [[PubMed](#)]
6. Huyer, L.D.; Pascual-Gil, S.; Wang, Y.; Mandla, S.; Yee, B.; Radisic, M. Advanced Strategies for Modulation of the Material–Macrophage Interface. *Adv. Funct. Mater.* **2020**, *30*, 1909331. [[CrossRef](#)]
7. Wolf, M.T.; Dearth, C.L.; Ranallo, C.A.; LoPresti, S.T.; Carey, L.E.; Daly, K.A.; Brown, B.N.; Badylak, S.F. Macrophage polarization in response to ECM coated polypropylene mesh. *Biomaterials* **2014**, *35*, 6838–6849. [[CrossRef](#)]
8. Bitar, D.; Parvizi, J. Biological response to prosthetic debris. *World J. Orthop.* **2015**, *6*, 172–189. [[CrossRef](#)]
9. Perez-Maceda, B.; López-Fernández, M.; Díaz, I.; Kavanaugh, A.; Billi, F.; Escudero, M.; García-Alonso, M.; Lozano, R. Macrophage Biocompatibility of CoCr Wear Particles Produced under Polarization in Hyaluronic Acid Aqueous Solution. *Materials* **2018**, *11*, 756. [[CrossRef](#)]
10. Escudero, M.L.; Llorente, I.; Pérez-Maceda, B.T.; San José-Pinilla, S.; Sánchez-López, L.; Lozano, R.M.; Aguado-Henche, S.; Clemente de Arriba, C.C.; Alobera-Gracia, M.A.; García-Alonso, M.C. Electrochemically reduced graphene oxide on CoCr biomedical alloy: Characterization, macrophage biocompatibility and hemocompatibility in rats with graphene and graphene oxide. *Mater. Sci. Eng. C* **2020**, *109*, 110522. [[CrossRef](#)]
11. Chico, B.; Pérez-Maceda, B.; José, S.S.; Escudero, M.; García-Alonso, M.; Lozano, R.M. Corrosion Behaviour and J774A.1 Macrophage Response to Hyaluronic Acid Functionalization of Electrochemically Reduced Graphene Oxide on Biomedical Grade CoCr. *Metals* **2021**, *11*, 1078. [[CrossRef](#)]
12. García-Argumán, A.; Llorente, I.; Caballero-Calero, O.; González, Z.; Menéndez, R.; Escudero, M.L.; García-Alonso, M.C. Electrochemical reduction of graphene oxide on biomedical grade CoCr alloy'. *Appl. Surf. Sci.* **2019**, *465*, 1028–1036. [[CrossRef](#)]
13. Mazzucco, D.; Scott, R.; Spector, M. Composition of joint fluid in patients undergoing total knee replacement and revision arthroplasty: Correlation with flow properties. *Biomaterials* **2004**, *25*, 4433–4445. [[CrossRef](#)] [[PubMed](#)]
14. Käll, L.; Canterbury, J.; Weston, J.; Noble, W.; MacCoss, M.J. Semi-supervised learning for peptide identification from shotgun proteomics datasets. *Nat. Methods* **2007**, *4*, 923–925. [[CrossRef](#)] [[PubMed](#)]
15. SRplot—Free Online Two or Three Way Venn Diagram. Available online: http://www.bioinformatics.com.cn/plot_basic_proportional_2_or_3_venn_diagram_028_en (accessed on 3 May 2022).
16. Aguilan, J.T.; Kulej, K.; Sidoli, S. Guide for protein fold change and p-value calculation for non-experts in proteomics. *Mol. Omics* **2020**, *16*, 573–582. [[CrossRef](#)]
17. Ge, S.X.; Jung, D.; Yao, R. ShinyGO: A graphical gene-set enrichment tool for animals and plants. *Bioinformatics* **2020**, *36*, 2628–2629. [[CrossRef](#)] [[PubMed](#)]
18. Lozano, R.M.; Pérez-Maceda, B.T.; Carboneras, M.; Onofre-Bustamante, E.; García-Alonso, M.C.; Escudero, M.L. Response of MC3T3-E1 osteoblasts, L929 fibroblasts, and J774 macrophages to fluoride surface-modified AZ31 magnesium alloy. *J. Biomed. Mater. Res. A* **2013**, *101*, 2753–2762. [[CrossRef](#)]
19. Brauer, A.; Pohlemann, T.; Metzger, W. Osteogenic differentiation of immature osteoblasts: Interplay of cell culture media and supplements. *Biotech. Histochem.* **2016**, *91*, 161–169. [[CrossRef](#)]
20. Brash, J.L.; Horbett, T.; Latour, R.; Tengvall, P. The blood compatibility challenge. Part 2: Protein adsorption phenomena governing blood reactivity. *Acta Biomater.* **2019**, *94*, 11–24. [[CrossRef](#)]
21. Milleret, V.; Buzzi, S.; Gehrig, P.; Ziogas, A.; Grossmann, J.; Schilcher, K.; Zinkernagel, A.S.; Zucker, A.; Ehrbar, M. Protein adsorption steers blood contact activation on engineered cobalt chromium alloy oxide layers. *Acta Biomater.* **2015**, *24*, 343–351. [[CrossRef](#)]
22. Sun, D.H.; Trindade, M.C.; Nakashima, Y.; Maloney, W.J.; Goodman, S.B.; Schurman, D.J.; Smith, R.L. Human serum opsonization of orthopedic biomaterial particles: Protein-binding and monocyte/macrophage activation in vitro. *J. Biomed. Mater. Res.* **2003**, *65*, 290–298. [[CrossRef](#)]
23. Wiegner, R.; Chakraborty, S.; Huber-Lang, M. Complement-coagulation crosstalk on cellular and artificial surfaces. *Immunobiology* **2016**, *221*, 1073–1079. [[CrossRef](#)] [[PubMed](#)]
24. Kim, J. Systematic approach to characterize the dynamics of protein adsorption on the surface of biomaterials using proteomics. *Colloids Surf. B Biointerfaces* **2020**, *188*, 110756. [[CrossRef](#)] [[PubMed](#)]
25. Samet, J.M.; Chen, H.; Pennington, E.; Bromberg, P.A. Non-redox cycling mechanisms of oxidative stress induced by PM metals. *Free Radic. Biol. Med.* **2020**, *151*, 26–37. [[CrossRef](#)]
26. Croom, E. Metabolism of Xenobiotics of Human Environments. In *Progress in Molecular Biology and Translational Science*, 112; Elsevier: Amsterdam, The Netherlands, 2012; pp. 31–88. [[CrossRef](#)]
27. Balali-Mood, M.; Naseri, K.; Tahergorabi, Z.; Khazdair, M.; Sadeghi, M. Toxic Mechanisms of Five Heavy Metals: Mercury, Lead, Chromium, Cadmium, and Arsenic. *Front. Pharmacol.* **2021**, *12*, 643972. [[CrossRef](#)] [[PubMed](#)]
28. Kovač, V.; Bergant, M.; Ščančar, J.; Primožič, J.; Jamnik, P.; Poljšak, B. Causation of Oxidative Stress and Defense Response of a Yeast Cell Model after Treatment with Orthodontic Alloys Consisting of Metal Ions. *Antioxidants* **2021**, *11*, 63. [[CrossRef](#)] [[PubMed](#)]
29. Canaparo, R.; Foglietta, F.; Limongi, T.; Serpe, L. Biomedical Applications of Reactive Oxygen Species Generation by Metal Nanoparticles. *Materials* **2020**, *14*, 53. [[CrossRef](#)] [[PubMed](#)]

30. Scharf, B.; Clement, C.C.; Zolla, V.; Perino, G.; Yan, B.; Elci, S.G.; Purdue, E.; Goldring, S.; Macaluso, F.; Cobelli, N.; et al. Molecular analysis of chromium and cobalt-related toxicity. *Sci. Rep.* **2015**, *4*, 5729. [[CrossRef](#)]
31. Valko, M.; Jomova, K.; Rhodes, C.; Kuča, K.; Musilek, K. Redox- and non-redox-metal-induced formation of free radicals and their role in human disease. *Arch. Toxicol.* **2016**, *90*, 1–37. [[CrossRef](#)]
32. Juan, C.A.; de la Lastra, J.P.; Plou, F.; Pérez-Lebeña, E. The Chemistry of Reactive Oxygen Species (ROS) Revisited: Outlining Their Role in Biological Macromolecules (DNA, Lipids and Proteins) and Induced Pathologies. *Int. J. Mol. Sci.* **2021**, *22*, 4642. [[CrossRef](#)]
33. Valko, M.; Jomova, K.; Rhodes, C.J.; Kuča, K.; Musilek, K. A proteome-wide assessment of the oxidative stress paradigm for metal and metal-oxide nanomaterials in human macrophages. *NanoImpact* **2020**, *17*, 100194. [[CrossRef](#)]
34. Pemmari, A.; Leppänen, T.; Paukkeri, E.-L.; Eskelinen, A.; Moilanen, T.; Moilanen, E. Gene expression in adverse reaction to metal debris around metal-on-metal arthroplasty: An RNA-Seq-based study. *J. Trace Elem. Med. Biol.* **2018**, *48*, 149–156. [[CrossRef](#)] [[PubMed](#)]
35. Naito, Y.; Takagi, T.; Higashimura, Y. Heme oxygenase-1 and anti-inflammatory M2 macrophages. *Arch. Biochem. Biophys.* **2014**, *564*, 83–88. [[CrossRef](#)] [[PubMed](#)]
36. Wegiel, B.; Nemeth, Z.; Correa-Costa, M.; Bulmer, A.; Otterbein, L.E. Heme Oxygenase-1: A Metabolic Nike. *Antioxid. Redox Signal.* **2014**, *20*, 1709–1722. [[CrossRef](#)] [[PubMed](#)]
37. Kirkby, K.A.; Adin, C.A. Products of heme oxygenase and their potential therapeutic applications. *Am. J. Physiol. Ren. Physiol.* **2006**, *290*, F563–F571. [[CrossRef](#)]
38. Kobayashi, E.H.; Suzuki, T.; Funayama, R.; Nagashima, T.; Hayashi, M.; Sekine, H.; Tanaka, N.; Moriguchi, T.; Motohashi, H.; Nakayama, K.; et al. Nrf2 suppresses macrophage inflammatory response by blocking proinflammatory cytokine transcription. *Nat. Commun.* **2016**, *7*, 11624. [[CrossRef](#)] [[PubMed](#)]
39. Zhang, M.; An, C.; Gao, Y.; Leak, R.; Chen, J.; Zhang, F. Emerging roles of Nrf2 and phase II antioxidant enzymes in neuroprotection. *Prog. Neurobiol.* **2013**, *100*, 30–47. [[CrossRef](#)]
40. Janasik, B.; Reszka, E.; Stanislawska, M.; Jablonska, E.; Kuras, R.; Wiczorek, E.; Malachowska, B.; Fendler, W.; Wasowicz, W. Effect of Arsenic Exposure on NRF2-KEAP1 Pathway and Epigenetic Modification. *Biol. Trace Elem. Res.* **2018**, *185*, 11–19. [[CrossRef](#)] [[PubMed](#)]
41. Ishii, T.; Itoh, K.; Takahashi, S.; Sato, H.; Yanagawa, T.; Katoh, Y.; Bannai, S.; Yamamoto, M. Transcription Factor Nrf2 Coordinately Regulates a Group of Oxidative Stress-inducible Genes in Macrophages. *J. Biol. Chem.* **2000**, *275*, 16023–16029. [[CrossRef](#)] [[PubMed](#)]
42. Kadl, A.; Meher, A.K.; Sharma, P.R.; Lee, M.Y.; Doran, A.C.; Johnstone, S.R.; Elliott, M.R.; Gruber, F.; Han, J.; Chen, W.; et al. Identification of a Novel Macrophage Phenotype That Develops in Response to Atherogenic Phospholipids via Nrf2'. *Circ. Res.* **2010**, *107*, 737–746. [[CrossRef](#)] [[PubMed](#)]
43. Chen, Q.; Wang, N.; Zhu, M.; Lu, J.; Zhong, H.; Xue, X.; Guo, S.; Li, M.; Wei, X.; Tao, Y.; et al. TiO₂ nanoparticles cause mitochondrial dysfunction, activate inflammatory responses, and attenuate phagocytosis in macrophages: A proteomic and metabolomic insight. *Redox Biol.* **2018**, *15*, 266–276. [[CrossRef](#)]
44. Abulikemu, A.; Zhao, X.; Qi, Y.; Liu, Y.; Wang, J.; Zhou, W.; Duan, H.; Li, Y.; Sun, Z.; Guo, C. Lysosomal impairment-mediated autophagy dysfunction responsible for the vascular endothelial apoptosis caused by silica nanoparticle via ROS/PARP1/AIF signaling pathway. *Environ. Pollut.* **2022**, *304*, 119202. [[CrossRef](#)]
45. McMahon, H.T.; Boucrot, E. Molecular mechanism and physiological functions of clathrin-mediated endocytosis. *Nat. Rev. Mol. Cell Biol.* **2011**, *12*, 517–533. [[CrossRef](#)]
46. Mu, Q.; Su, G.; Li, L.; Gilbertson, B.O.; Yu, L.H.; Zhang, Q.; Sun, Y.P.; Yan, B. Size-Dependent Cell Uptake of Protein-Coated Graphene Oxide Nanosheets. *ACS Appl. Mater. Interfaces* **2012**, *4*, 2259–2266. [[CrossRef](#)] [[PubMed](#)]
47. Donahue, N.D.; Acar, H.; Wilhelm, S. Concepts of nanoparticle cellular uptake, intracellular trafficking, and kinetics in nanomedicine. *Adv. Drug Deliv. Rev.* **2019**, *143*, 68–96. [[CrossRef](#)] [[PubMed](#)]
48. Sánchez-López, L.; Chico, B.; Llorente, I.; Escudero, M.; Lozano, R.; García-Alonso, M.C. Covalent immobilization of graphene oxide on biomedical grade CoCr alloy by an improved multilayer system assembly via Silane/GO bonding. *Mater. Chem. Phys.* **2022**, *287*, 126296. [[CrossRef](#)]
49. Yue, H.; Wei, W.; Yue, Z.; Wang, B.; Luo, N.; Gao, Y.; Ma, D.; Ma, G.; Su, Z. The role of the lateral dimension of graphene oxide in the regulation of cellular responses. *Biomaterials* **2012**, *33*, 4013–4021. [[CrossRef](#)]
50. Behzadi, S.; Serpooshan, V.; Tao, W.; Hamaly, M.A.; Alkawareek, M.Y.; Dreaden, E.C.; Brown, D.; Alkilany, A.M.; Farokhzad, O.C.; Mahmoudi, M. Cellular uptake of nanoparticles: Journey inside the cell. *Chem. Soc. Rev.* **2017**, *46*, 4218–4244. [[CrossRef](#)]
51. Kawai, T.; Akira, S. Signaling to NF- κ B by Toll-like receptors. *Trends Mol. Med.* **2007**, *13*, 460–469. [[CrossRef](#)]
52. Ma, J.; Liu, R.; Wang, X.; Liu, Q.; Chen, Y.; Valle, R.P.; Zuo, Y.Y.; Xia, T.; Liu, S. Crucial Role of Lateral Size for Graphene Oxide in Activating Macrophages and Stimulating Pro-inflammatory Responses in Cells and Animals. *ACS Nano* **2015**, *9*, 10498–10515. [[CrossRef](#)]
53. Chen, G.Y.; Yang, H.J.; Lu, C.H.; Chao, Y.C.; Hwang, S.M.; Chen, C.L.; Lo, K.W.; Sung, L.Y.; Luo, W.Y.; Tuan, H.Y.; et al. Simultaneous induction of autophagy and toll-like receptor signaling pathways by graphene oxide. *Biomaterials* **2012**, *33*, 6559–6569. [[CrossRef](#)]

54. Mukherjee, S.P.; Bondarenko, O.; Kohonen, P.; Andón, F.T.; Brzicová, T.; Gessner, I.; Mathur, S.; Bottini, M.; Calligari, P.; Stella, L.; et al. Macrophage sensing of single-walled carbon nanotubes via Toll-like receptors. *Sci. Rep.* **2018**, *8*, 1115. [[CrossRef](#)] [[PubMed](#)]
55. Xiaoli, F.; Yaqing, Z.; Ruhui, L.; Xuan, L.; Aijie, C.; Yanli, Z.; Chen, H.; Lili, C.; Longquan, S. Graphene oxide disrupted mitochondrial homeostasis through inducing intracellular redox deviation and autophagy-lysosomal network dysfunction in SH-SY5Y cells. *J. Hazard. Mater.* **2021**, *416*, 126158. [[CrossRef](#)] [[PubMed](#)]
56. Zhang, B.; Wei, P.; Zhou, Z.; Wei, T. Interactions of graphene with mammalian cells: Molecular mechanisms and biomedical insights. *Adv. Drug Deliv. Rev.* **2016**, *105*, 145–162. [[CrossRef](#)] [[PubMed](#)]
57. Zhou, T.; Zhang, B.; Wei, P.; Du, Y.; Zhou, H.; Yu, M.; Yan, L.; Zhang, W.; Nie, G.; Chen, C.; et al. Energy metabolism analysis reveals the mechanism of inhibition of breast cancer cell metastasis by PEG-modified graphene oxide nanosheets. *Biomaterials* **2014**, *35*, 9833–9843. [[CrossRef](#)] [[PubMed](#)]
58. Zhou, H.; Zhang, B.; Zheng, J.; Yu, M.; Zhou, T.; Zhao, K.; Jia, Y.; Gao, X.; Chen, C.; Wei, T. The inhibition of migration and invasion of cancer cells by graphene via the impairment of mitochondrial respiration. *Biomaterials* **2014**, *35*, 1597–1607. [[CrossRef](#)] [[PubMed](#)]
59. Svadlakova, T.; Hubatka, F.; Turanek Knotigova, P.; Kulich, P.; Masek, J.; Kotoucek, J.; Macak, J.; Motola, M.; Kalbac, M.; Kolackova, M.; et al. Proinflammatory Effect of Carbon-Based Nanomaterials: In Vitro Study on Stimulation of Inflammasome NLRP3 via Destabilisation of Lysosomes. *Nanomaterials* **2020**, *10*, 418. [[CrossRef](#)] [[PubMed](#)]
60. Lord, M.S.; Melrose, J.; Day, A.; Whitelock, J.M. The Inter- α -Trypsin Inhibitor Family: Versatile Molecules in Biology and Pathology. *J. Histochem. Cytochem.* **2020**, *68*, 907–927. [[CrossRef](#)]
61. Lee-Sayer, S.S.M.; Dong, Y.; Arif, A.A.; Olsson, M.; Brown, K.L.; Johnson, P. The Where, When, How, and Why of Hyaluronan Binding by Immune Cells. *Front. Immunol.* **2015**, *6*, 150. [[CrossRef](#)]
62. Chen, Y.; Zhang, B.; Yu, L.; Zhang, J.; Zhao, Y.; Yao, L.; Yan, H.; Tian, W. A novel nanoparticle system targeting damaged mitochondria for the treatment of Parkinson's disease. *Biomater. Adv.* **2022**, *138*, 212876. [[CrossRef](#)]
63. Kotla, N.G.; Bonam, S.R.; Rasala, S.; Wankar, J.; Bohara, R.A.; Bayry, J.; Rochev, Y.; Pandit, A. Recent advances and prospects of hyaluronan as a multifunctional therapeutic system. *J. Control. Release* **2021**, *336*, 598–620. [[CrossRef](#)]
64. Campo, G.M.; Avenoso, A.; Nastasi, G.; Micali, A.; Prestipino, V.; Vaccaro, M.; D'Ascola, A.; Calatroni, A.; Campo, S. Hyaluronan reduces inflammation in experimental arthritis by modulating TLR-2 and TLR-4 cartilage expression. *Biochim. Biophys. Acta BBA Mol. Basis Dis.* **2011**, *1812*, 1170–1181. [[CrossRef](#)] [[PubMed](#)]
65. Wang, C.-T.; Lin, Y.-T.; Chiang, B.-L.; Lin, Y.-H.; Hou, S.-M. High molecular weight hyaluronic acid down-regulates the gene expression of osteoarthritis-associated cytokines and enzymes in fibroblast-like synoviocytes from patients with early osteoarthritis. *Osteoarthr. Cartil.* **2006**, *14*, 1237–1247. [[CrossRef](#)] [[PubMed](#)]
66. Rayahin, J.E.; Buhman, J.S.; Zhang, Y.; Koh, T.J.; Gemeinhart, R.A. High and Low Molecular Weight Hyaluronic Acid Differentially Influence Macrophage Activation. *ACS Biomater. Sci. Eng.* **2015**, *1*, 481–493. [[CrossRef](#)] [[PubMed](#)]
67. Xu, J.; Chi, F.; Guo, T.; Punj, V.; Lee, W.P.; French, S.W.; Tsukamoto, H. NOTCH reprograms mitochondrial metabolism for proinflammatory macrophage activation. *J. Clin. Investig.* **2015**, *125*, 1579–1590. [[CrossRef](#)]
68. Battiston, K.G.; Labow, R.S.; Santerre, J.P. Protein binding mediation of biomaterial-dependent monocyte activation on a degradable polar hydrophobic ionic polyurethane. *Biomaterials* **2012**, *33*, 8316–8328. [[CrossRef](#)] [[PubMed](#)]
69. Jin, H.; Tian, L.; Bing, W.; Zhao, J.; Ren, L. Toward the Application of Graphene for Combating Marine Biofouling. *Adv. Sustain. Syst.* **2021**, *5*, 2000076. [[CrossRef](#)]
70. Mahdavi, H.; Rahimi, A. Zwitterion functionalized graphene oxide/polyamide thin film nanocomposite membrane: Towards improved anti-fouling performance for reverse osmosis. *Desalination* **2018**, *433*, 94–107. [[CrossRef](#)]
71. Ayyaru, S.; Ahn, Y.-H. Application of sulfonic acid group functionalized graphene oxide to improve hydrophilicity, permeability, and antifouling of PVDF nanocomposite ultrafiltration membranes. *J. Membr. Sci.* **2017**, *525*, 210–219. [[CrossRef](#)]
72. Ali, M.E.; Wang, L.; Wang, X.; Feng, X. Thin film composite membranes embedded with graphene oxide for water desalination. *Desalination* **2016**, *386*, 67–76. [[CrossRef](#)]
73. Singla, D.K.; Wang, J.; Singla, R. Primary human monocytes differentiate into M2 macrophages and involve Notch-1 pathway. *Can. J. Physiol. Pharmacol.* **2017**, *95*, 288–294. [[CrossRef](#)]
74. Araújo-Gomes, N.; Romero-Gavilán, F.; Zhang, Y.; Martínez-Ramos, C.; Elortza, F.; Azkargorta, M.; DE Llano, J.J.M.; Gurruchaga, M.; Goñi, I.; Beucken, J.V.D.; et al. Complement proteins regulating macrophage polarisation on biomaterials. *Colloids Surfaces B Biointerfaces* **2019**, *181*, 125–133. [[CrossRef](#)] [[PubMed](#)]
75. Asgari, E.; Le Fric, G.; Yamamoto, H.; Perucha, E.; Sacks, S.; Koehl, J.; Cook, H.T.; Kemper, C. C3a modulates IL-1 β secretion in human monocytes by regulating ATP efflux and subsequent NLRP3 inflammasome activation. *Blood* **2013**, *122*, 3473–3481. [[CrossRef](#)] [[PubMed](#)]
76. Nilsson, B.; Ekdahl, K.N.; Mollnes, T.E.; Lambris, J.D. The role of complement in biomaterial-induced inflammation. *Mol. Immunol.* **2007**, *44*, 82–94. [[CrossRef](#)] [[PubMed](#)]
77. Page, M.J.; Bester, J.; Pretorius, E. The inflammatory effects of TNF- α and complement component 3 on coagulation. *Sci. Rep.* **2018**, *8*, 1812. [[CrossRef](#)]
78. Tan, H.-Y.; Wang, N.; Li, S.; Hong, M.; Wang, X.; Feng, Y. The Reactive Oxygen Species in Macrophage Polarization: Reflecting Its Dual Role in Progression and Treatment of Human Diseases. *Oxid. Med. Cell. Longev.* **2016**, *2016*, 2795090. [[CrossRef](#)] [[PubMed](#)]

79. Liu, C.; Hu, F.; Jiao, G.; Guo, Y.; Zhou, P.; Zhang, Y.; Zhang, Z.; Yi, J.; You, Y.; Li, Z.; et al. Dental pulp stem cell-derived exosomes suppress M1 macrophage polarization through the ROS-MAPK-NF κ B P65 signaling pathway after spinal cord injury. *J. Nanobiotechnol.* **2022**, *20*, 65. [[CrossRef](#)] [[PubMed](#)]
80. Liu, T.; Zhang, L.; Joo, D.; Sun, S.-C. NF- κ B signaling in inflammation. *Signal Transduct. Target. Ther.* **2017**, *2*, 17023. [[CrossRef](#)]
81. López-Zambrano, M.; Rodríguez-Montesinos, J.; Crespo-Avilan, G.E.; Muñoz-Vega, M.; Preissner, K.T. Thrombin Promotes Macrophage Polarization into M1-Like Phenotype to Induce Inflammatory Responses. *Thromb. Haemost.* **2020**, *120*, 658–670. [[CrossRef](#)]
82. Kazezian, Z.; Joyce, K.; Pandit, A. The Role of Hyaluronic Acid in Intervertebral Disc Regeneration. *Appl. Sci.* **2020**, *10*, 6257. [[CrossRef](#)]
83. Onodera, Y.; Teramura, T.; Takehara, T.; Fukuda, K. Hyaluronic acid regulates a key redox control factor Nrf2 via phosphorylation of Akt in bovine articular chondrocytes. *FEBS Open Bio* **2015**, *5*, 476–484. [[CrossRef](#)]
84. Yu, C.-J.; Ko, C.-J.; Hsieh, C.-H.; Chien, C.-T.; Huang, L.-H.; Lee, C.-W.; Jiang, C.-C. Proteomic analysis of osteoarthritic chondrocyte reveals the hyaluronic acid-regulated proteins involved in chondroprotective effect under oxidative stress. *J. Proteom.* **2014**, *99*, 40–53. [[CrossRef](#)]
85. Pauloin, T.; Dutot, M.; Warnet, J.-M.; Rat, P. In vitro modulation of preservative toxicity: High molecular weight hyaluronan decreases apoptosis and oxidative stress induced by benzalkonium chloride. *Eur. J. Pharm. Sci.* **2008**, *34*, 263–273. [[CrossRef](#)]
86. Wu, W.; Jiang, H.; Guo, X.; Wang, Y.; Ying, S.; Feng, L.; Li, T.; Xia, H.; Zhang, Y.; Chen, R.; et al. The Protective Role of Hyaluronic Acid in Cr(VI)-Induced Oxidative Damage in Corneal Epithelial Cells. *J. Ophthalmol.* **2017**, *2017*, 3678586. [[CrossRef](#)]
87. Takasugi, M.; Firsanov, D.; Tomblin, G.; Ning, H.; Ablava, J.; Seluanov, A.; Gorbunova, V. Naked mole-rat very-high-molecular-mass hyaluronan exhibits superior cytoprotective properties. *Nat. Commun.* **2020**, *11*, 2376. [[CrossRef](#)] [[PubMed](#)]
88. Gorbunova, V.; Takasugi, M.; Seluanov, A. Hyaluronan goes to great length. *Cell Stress* **2020**, *4*, 227–229. [[CrossRef](#)] [[PubMed](#)]
89. Xu, C.; Shi, Q.; Zhang, L.; Zhao, H. High molecular weight hyaluronan attenuates fine particulate matter-induced acute lung injury through inhibition of ROS-ASK1-p38/JNK-mediated epithelial apoptosis. *Environ. Toxicol. Pharmacol.* **2018**, *59*, 190–198. [[CrossRef](#)] [[PubMed](#)]
90. Tan, A.S.; Berridge, M.V. Superoxide produced by activated neutrophils efficiently reduces the tetrazolium salt, WST-1 to produce a soluble formazan: A simple colorimetric assay for measuring respiratory burst activation and for screening anti-inflammatory agents. *J. Immunol. Methods* **2000**, *238*, 59–68. [[CrossRef](#)]
91. Peskin, A.V.; Winterbourn, C.C. A microtiter plate assay for superoxide dismutase using a water-soluble tetrazolium salt (WST-1). *Clin. Chim. Acta* **2000**, *293*, 157–166. [[CrossRef](#)]
92. Hameister, R.; Lohmann, C.H.; Dheen, S.T.; Singh, G.; Kaur, C. The effect of TNF- α on osteoblasts in metal wear-induced periprosthetic bone loss. *Bone Jt. Res.* **2020**, *9*, 827–839. [[CrossRef](#)]
93. Jonitz-Heincke, A.; Sellin, M.-L.; Seyfarth, A.; Peters, K.; Mueller-Hilke, B.; Fiedler, T.; Bader, R.; Klinder, A. Analysis of Cellular Activity and Induction of Inflammation in Response to Short-Term Exposure to Cobalt and Chromium Ions in Mature Human Osteoblasts. *Materials* **2019**, *12*, 2771. [[CrossRef](#)]
94. Salloum, Z.; Lehoux, E.A.; Harper, M.-E.; Catelas, I. Effects of cobalt and chromium ions on oxidative stress and energy metabolism in macrophages in vitro. *J. Orthop. Res.* **2018**, *36*, 3178–3187. [[CrossRef](#)] [[PubMed](#)]
95. Jarosz, A.; Skoda, M.; Dudek, I.; Szukiewicz, D. Oxidative Stress and Mitochondrial Activation as the Main Mechanisms Underlying Graphene Toxicity against Human Cancer Cells. *Oxid. Med. Cell. Longev.* **2015**, *2016*, 5851035. [[CrossRef](#)] [[PubMed](#)]
96. Berridge, M.V.; Herst, P.M.; Tan, A.S. Tetrazolium dyes as tools in cell biology: New insights into their cellular reduction. *Biotechnol. Annu. Review.* **2005**, *11*, 127–152. [[CrossRef](#)]
97. Scarcello, E.; Lambremont, A.; Vanbever, R.; Jacques, P.J.; Lison, D. Mind your assays: Misleading cytotoxicity with the WST-1 assay in the presence of manganese. *PLoS ONE* **2020**, *15*, e0231634. [[CrossRef](#)] [[PubMed](#)]

Disclaimer/Publisher’s Note: The statements, opinions and data contained in all publications are solely those of the individual author(s) and contributor(s) and not of MDPI and/or the editor(s). MDPI and/or the editor(s) disclaim responsibility for any injury to people or property resulting from any ideas, methods, instructions or products referred to in the content.